Concrete and Steel Bridges

8 reports prepared for the 54th Annual Meeting
of the Transportation Research Board

The conference that is the subject of this report was approved by the Governing Board of the National Research Council acting in behalf of the National Academy of Sciences. Such approval reflects the Governing Board's judgment that the conference is of national importance and appropriate with respect to both the purposes and resources of the National Research Council.

The members of the committee selected to organize the conference and to supervise the preparation of the report were chosen for recognized scholarly competence and with due consideration for the balance of disciplines appropriate to the project.

Responsibility for the selection of the participants in the conference and for any summaries or recommendations in this report rests with that committee. The views expressed in individual papers and attributed to the authors of those papers are those of the authors and do not necessarily reflect the view of the committee, the Transportation Research Board, the National Academy of Sciences, or the sponsors of the project.

Each report issuing from such a conference of the National Research Council is reviewed by an independent group of qualified individuals according to procedures established and monitored by the Report Review Committee of the National Academy of Sciences. Distribution of the report is approved by the President of the Academy upon satisfactory completion of the review process.

CONTENTS

FOREWORD

The papers in this RECORD are oriented primarily toward the interests of the bridge designer. They also may be of interest to the researcher. Some may be of use to bridge maintenance and administration groups. Interesting findings and information are presented for both steel and concrete bridges.

Carpenter et al. present an abbreviation of results of a study on design of pier caps. The study results were confirmed by tests on scale models of bridges, and significant reductions in reinforcement bar requirements were found.

Heins deals with the design of horizontally curved, simple-span, multiple I-girder bridges. His approach to solving a design problem is direct. He presents a means of determining amplification factors that can then be applied to moments and shears that have been determined in conventional ways for a straight-girder bridge.

Radolli and Green studied effects of the sun on stresses in reinforced concrete bridges. Appraisals were made combining heat-flow theory with structural analysis, and surprisingly high stresses were predicted, especially for deep concrete girders of continuous design. These stresses were not considered great enough to affect structural safety, but they were considered to be significant in causing cracking and reducing service life of the structure. Proper reinforcement should be performed to distribute cracking. Guidelines for this are presented.

Huang presents a direct method for predicting prestress losses in prestressed concrete bridge girders. The proposed technique permits rather accurate prediction of losses. The technique retains the relative simplicity of earlier, cruder approximations.

Davis and Castleton uncover some peculiarities of steel box-girder behavior under load by means of a field test. They used sophisticated testing and recording procedures and corroborated their results by finite element analysis. They conclude that so many factors affect box-girder behavior that a rigorous computer analysis, rather than simple approximations of loads and stress distributions, should be used.

Crozier et al. give some interesting results of tests on reinforced, elastomeric bridge bearing pads. All pads were reinforced by layers of steel, fiberglass, or polyester cloth. Full-size specimens were loaded in simulated service conditions. Steel and fiberglass reinforcement showed decided superiority.

Conley, Kaltenhauser, and Klaphake provide details on a computer program devised for easy storage and retrieval of bridge inventory information. The program has been found helpful in preparing reports, budgetary studies, and maintenance schedules and in other bridge department activities.

Thornton discusses the problem of staining bridge piers. He provides information on the causes, composition, and cures that should be of interest. The paper summarizes survey responses on experiences in the United States and presents practices that have been found effective in countering various problems.

—George W. Zuurbier

DESIGN OF BENT CAPS FOR
CONCRETE BOX-GIRDER BRIDGES

James E. Carpenter, Anthony E. Fiorato, and Henry G. Russell,
   Portland Cement Association; and
John M. Hanson,* Wiss, Janney, Elstner and Associates

ABRIDGMENT

Design recommendations for integral bent caps in straight, continuously reinforced concrete box-girder bridges were developed from the results of an experimental and analytical investigation. The results indicate that, in design, flexural reinforcement reductions of up to 40 percent can be made without reducing safety or adequate serviceability.

•DESIGN recommendations for integral bent caps in straight, continuously reinforced concrete box-girder bridges were developed from the results of an experimental and analytical investigation. The investigation was to determine whether certain assumptions and working-stress design methods in use in 1970 required more flexural reinforcement than necessary. This paper briefly summarizes the investigation and design recommendations. Further details are available elsewhere (1, 2, 3).

The results of the investigation indicate that, in design, flexural reinforcement reductions of up to 40 percent can be made without reducing safety or adequate serviceability. Even greater reductions in the amount of reinforcement can be made for bent caps with flared columns. Most of this improved economy results from changing from the working-stress to the load-factor method of design.

INVESTIGATION

Studies were conducted on distribution of loads on the bent cap, effect of flaring the column in the plane of the bent, effective flange width of the bent cap in tension and compression, effect of spreading main tensile reinforcement into the adjacent superstructure, and location of critical design sections.

Experimental tests were conducted on two $\frac{1}{5}$-scale models of complete box-girder bridges, four $\frac{2}{5}$-scale models of single-column bent-cap portions of the bridges, and one $\frac{1}{5}$-scale model of a double-column bent-cap portion of a bridge. The model of a complete bridge with a single-column bent is shown in Figure 1.

Analytical studies included development of 2 computer programs. One used the elastic folded-plate method to predict the load-carrying mechanism of the complete bridges. The other used the finite element method to simulate in detail the behavior of the bent cap. Details included simulation of cracking of concrete and yielding of reinforcement.
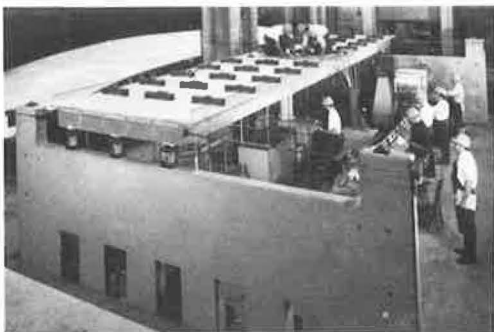
TEST RESULTS

Results from tests of the 2 complete model bridges indicated that, at loads approaching

---

*Mr. Hanson was with the Portland Cement Association when this research was performed.

Figure 1. Model single-column bridge ready for test.

ultimate, little load was transferred laterally from girder to girder. Analytical results, based on elastic material properties, predicted a somewhat greater lateral distribution of load. However, with or without this distribution, moments in the bent cap were found to be essentially the same. On the basis of these results, we recommend that the current design assumption of no lateral distribution of load be used.

Two bent caps with flared columns were tested; one had a flared support surface forming a 45-deg angle with the vertical, and the other had an intermediate flare forming a 27-deg angle with the vertical. Both flared columns were found to be fully effective as supports. Stresses induced in the concrete of the flare itself were not excessive. Reinforcement stresses in the bent cap were comparable with those at corresponding locations in a specimen with a cylindrical column. On the basis of these results, we recommend that all flares up to 45 deg be considered effective supports. Similar provisions already exist in building codes.
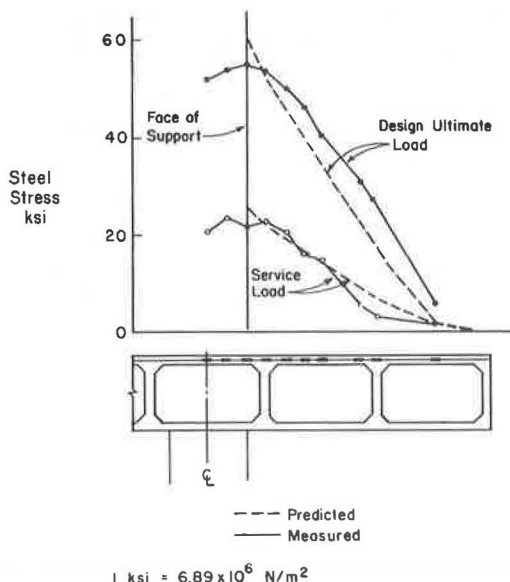
Existing provisions for compressive flange widths in box girders, restated for overhanging flanges, were found to apply to bent caps. For tension flanges, we recommend effective widths similar to those for compression flanges if the effective overhanging flange width is limited to a fourth of the box web spacing. This width ensures that reinforcement will not be overstressed by secondary effects.

The effectiveness of flexural reinforcement was found to diminish rapidly with increasing distance from the bent-cap web. However, we recommend that reinforcement that is spread only to the limits of the effective flange width in tension be considered completely effective.

The critical design section for negative moment in the bent caps was found to be at the face of the support. This section is the intersection of the extremity of the effective support with the bottom of the bent cap. The critical design section for positive moment was found to be at mid-span of the double-column bent.

For each of the bent-cap specimens, steel stresses predicted according to the recommendations in the report were compared with those measured. Representative results are shown in Figure 2 for the specimen with a single cylindrical column.

Comparisons were made at service and design ultimate load levels. At design ultimate load, measured stresses near the end of the bent cap exceeded predicted stresses. This is a familiar effect of diagonal cracking, which traditionally is accommodated by extending reinforcement beyond theoretical cutoff points. Near the face of support, measured stresses were lower than those predicted.

Figure 2. Measured and predicted stresses in bent cap.

ACKNOWLEDGMENTS

portation Officials in cooperation with the Federal Highway Administration and was conducted in the National Cooperative Highway Research Program.

The elastic folded-plate analysis was conducted by A. C. Scordelis of the University of California, Berkeley. The finite element analysis was conducted by P. P. Lynn and S. Arya at the University of Colorado. Credit is due to the many present and former members of the Portland Cement Association staff who contributed to the project.

The opinions and conclusions expressed or implied in this report are those of the authors. They are not necessarily those of the Transportation Research Board, the National Academy of Sciences, the Federal Highway Administration, the American Association of State Highway and Transportation Officials, or the individual states participating in the National Cooperative Highway Research Program.

REFERENCES

1. Analysis and Design of Bridge Bents. NCHRP Project 12-10, Final Rept.
2. J. E. Carpenter, J. M. Hanson, A. E. Fiorato, H. G. Russell, D. F. Meinheit, I. Rosenthal, W. G. Corley, and E. Hognestad. Design of Bent Caps for Concrete Box-Girder Bridges. Portland Cement Association, Skokie, Illinois, Bulletin RD-030.
3. Design of Bent Caps for Concrete Box Girder Bridges. NCHRP Research Results Digest 65, Nov. 1974.

CURVED I-GIRDER DESIGN

Conrad P. Heins, Jr., Civil Engineering Department, University of Maryland

Design data that permit rapid determination of the forces and stresses in curved bridges subjected to dead and live loads are presented. The data were developed during a recent comprehensive study on curved bridges. The data are applied in an example design.

•DURING the past 5 years there has been a trend toward designing and constructing horizontally curved highway bridges. This has created a need for methods by which such systems can be conveniently designed. Several methods have been developed to analyze curved bridge systems (1, 2, 3, 4, 5), but they are not design aids. Design aids have been obtained by using 2 analytical methods that accurately represent the response of the structural system under dead load (4) and live load (3, 5). The results are in design equations and graphs, which permits design of a curved composite girder structure. Thus the engineer can determine girder properties and diaphragm spacings before a trial-and-error analysis.

Effects of impact will be included in the presentation of the design data.

The notations used in the formulations in this paper are as follows:

Bi = induced bimoment (lateral flange bending effect),
b_f = flange width of steel girder,
C = distance from bending neutral axis to any fiber,
C_1 = bending stress correction factor = $\bar{S}/S$,
C_2 = warping stress correction factor = $(W_n/I_w)/(\overline{W_n/I_w})$,
E_c = modulus of elasticity of composite,
E_s = modulus of elasticity of steel,
f = function,
F = maximum function,
G_c = modulus of rigidity of composite,
G_s = modulus of rigidity of steel,
h = centerline distance between flanges of a steel I-girder,
I_f = flexural impact factor,
I_T = torsional impact factor,
I_w = warping torsional moment of inertia,
I_x = primary moment of inertia of girders (actual stiffness),
K = design factor,
K_1 = amplification factor,
K_2 = distribution factor,
K_3 = reduction factor,
K_T = Saint Venant's torsional rigidity,
L = span length,
m = G_c/G_s,
M = induced bending moment,
M_b = maximum forces in 4-curved-girder system,
M_x = internal bending moment,
n = E_c/E_s,

R = radius of curvature of curved girder,

S = section modulus spacing or radial diaphragm spacing,

$\overline{S}$ = wheel load factor,

w = uniform dead load applied along the span of each girder,

$W_n = b_f \cdot h/4$ = warping statical moment of steel girder section,

$\overline{W_n/I_w}$ = referenced value,

W_{n_c} = composite warping statical moment,

W_{n_s} = steel warping statical moment,

σ_b = normal stress (actual or corrected) in longitudinal direction of girder due to bending,

$\overline{\sigma}_b$ = bending stress from referenced properties,

σ_w = normal stress (actual or corrected) in longitudinal direction of girder due to warping, and

$\overline{\sigma}_w$ = warping stress from referenced properties.

GENERAL DESIGN DATA

To analyze curved girder systems, one must know the girder section properties I_x, K_T, and I_w. The designer, therefore, must estimate the size of the girders to compute these stiffnesses. This size estimation can be achieved if the primary internal girder forces M_x and Bi, which induce normal stresses, are known. Then the basic bending equation,

$$\sigma_b = \frac{M_x C}{I_x} = \frac{M_x}{(I_x/C)} \tag{1}$$

and warping equation,

$$\sigma_w = \frac{Bi W_n}{I_w} = \frac{Bi}{(I_w/W_n)} \tag{2}$$

could be applied by assuming a proportion of the design stress for σ_b and σ_w and computing the required (I_x/C) and (I_w/W_n) properties. Estimation of these stresses and forces has been obtained by performing a thorough system analysis of single-span and multispan curved bridges (4, 5).

Impact Factors

The dynamic response of single-span curved girder bridges subjected to a sprung mass vehicle was predicted by a Fourier series and lump-mass techniques (8). These techniques then were applied in determining the response of typical highway bridges. This evaluated impact factors. Partial results of these studies are shown in Figures 1 and 2 for plate girder bridges. Curves are given for various girder span lengths and central angles, $\theta = L/R$. The curves are for a vehicle speed of 60 mph (96 km/h); other curves are available for velocities of 20 and 40 mph (32 and 64 km/h) (8).

Impact factors are applied as in conventional practice:

$$M = M_{static}(1 + I_r) \tag{3}$$

$$Bi = Bi_{static}(1 + I_r) \tag{4}$$

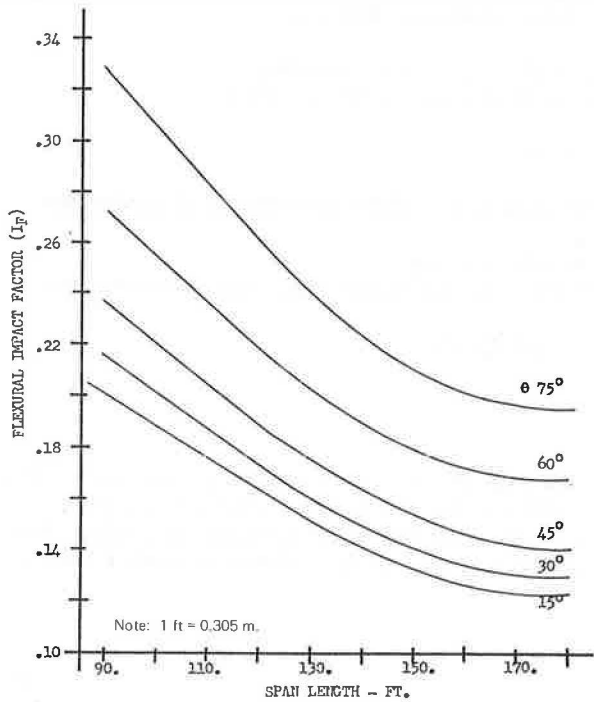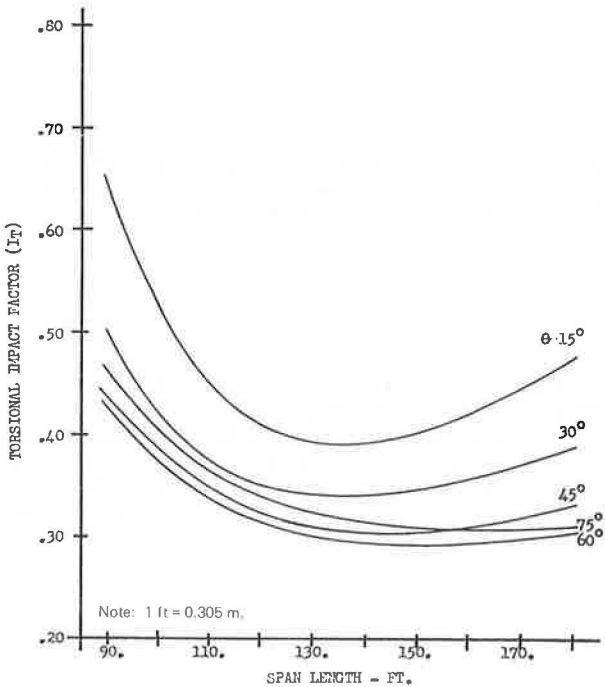**Figure 1. Flexural impact factor.**

Figure 2. Torsional impact factor.

Live Load Design

Design of any bridge element requires the establishment of forces in that element. If the bridge has a straight alignment, the forces can be determined by distribution factors and simple beam theory. However, when the structure is curved, the interaction of the bending and torsional forces creates an indeterminate situation. The following equations therefore were developed by using relationships between single curved responses and the system, to permit evaluation of the live load forces developed in a curved composite-bridge I-girder system (3, 5, 6, 7). These forces then can be used to establish the induced stresses and proper girder section.

Amplification Factor, K_1

All the internal forces and deformations for a single curved girder and a single straight girder have been evaluated by using various computer programs (6, 9). The ratio of the reactions for these 2 girders gives the following:

$$K_1 = \frac{f(\text{single curved girder})}{f(\text{single straight girder})} \tag{5}$$

This factor describes the immediate effect of curvature relative to a straight member. A graphical representation and analysis of these data give the following general equations:

$$K_{moment} = \frac{0.15}{n}(L/R) + 1 \tag{6}$$

$$K_{bimoment} = [(35n)(L/R)^2 - 15(L/R)] \times 10^3 \tag{7}$$

where $n = R/100$ [$R > 100$ ft (30.5 m)].

Distribution Factor, K_2

The evaluation of true distribution of load to each girder, and realistic values of internal forces, can be considered by analyzing the curved girder as a system. The number of trucks used in the analysis would depend on the number of lanes. The ratio of these resulting maximum forces to those in a single curved girder gives

$$K_2 = \frac{f(\text{system of curved girders})}{f(\text{single curved girder})} \tag{8}$$

A plot of this ratio versus R and L will yield the following general equations:

$$K_{moment} = (n + 3)\left(\frac{0.4L}{R}\right) + 0.6 \tag{9}$$

$$K_{bimoment} = \frac{0.11}{M}(R/L) \qquad L < 70 \text{ ft } (21.3 \text{ m})\tag{10}$$

$$K_{bimoment} = \frac{(M-1)}{6}(R/L) \qquad L > 70 \text{ ft } (21.3 \text{ m})\tag{11}$$

where

n = R/100 [R > 100 ft (30.5 m)], and
M = L/50 [L > 50 ft (15.25 m)].

These equations are valid for girder systems that contain 4, 6, and 8 girders and girder spacings of 7, 8, 9, and 10 ft (2.14, 2.44, 2.75, and 3.05 m).

Reduction Factor, K_3

Because many bridge structures are continuous, it is desirable to obtain some factors that can be applied to the simple span data to give preliminary forces in continuous spans. This factor can be written as

$$K_3 = \frac{f(\text{system of curved girders})N}{f(\text{system of curved girders})}\tag{12}$$

where N = number of spans.

Using a computer program, we evaluated the maximum forces in a 2- or 3-span curved bridge system of 4, 6, and 8 girders under various critical loadings. A study of all the data and the resulting K_3 values gives the values in Table 1. The data are described relative to number of spans and are independent of number of girders. It should be emphasized that the 2- and 3-span girder systems must contain equal span lengths with a maximum given span length of 100.0 ft (30.5 m). For example, for a 3-span system, the total maximum bridge length would then be 3 × L or 300.0 ft (91.5 m).

EVALUATION OF GIRDER FORCES AND DEFORMATION

With the various factor equations available, one can evaluate preliminary forces in a curved girder bridge, relative to the forces in a straight girder. (All Rs and Ls refer to the centerline of the bridge system.)

1. Evaluate F for a single straight girder of length L that has been subjected to a line of AASHO wheel loads. This function would be $F_{bending}$. The function for $F_{bimoment}$ is assumed to be equal to 1.
2. Evaluate K_1 equations 6 and 7 for L and R of the bridge system.
3. Evaluate K_2 equations 9, 10, and 11 for L, number of girders in system, and R.
4. Select a reduction factor from Table 1 if system is a continuous span.
5. Determine F of curved girder system, that is

$$\text{Maximum moment}_{static} = M_{straight} \times (K_1 \times K_2 \times K_3)\tag{13}$$

and

Table 1. Reduction factors for maximum bridge function.

Number of Spans	Bending Moment	Deflection	Rotation	Saint Venant	Warping Torsion	Bimoment	Shear
2	0.75	0.70	0.70	0.75	0.45	0.35	1.00
3	0.65	0.60	0.70	0.75	0.40	0.35	0.90

Figure 3. Section properties versus span length.

$$f_1 = -.4(10)^{-8}L^3 + .166(10)^{-5}L^2 - .230(10)^{-3}L + .112$$

(Plate Girder) $\quad f_2 = -.530(10)^{-9}L^3 + .249(10)^{-5}L^2 - 8.5(10)^{-3}L + .101$

$\left[\dfrac{Iv/\sqrt{n}}{Ix}\right]$ vs. Span Length

Note: 1 ft = 0.305 m.

L—Span (ft)
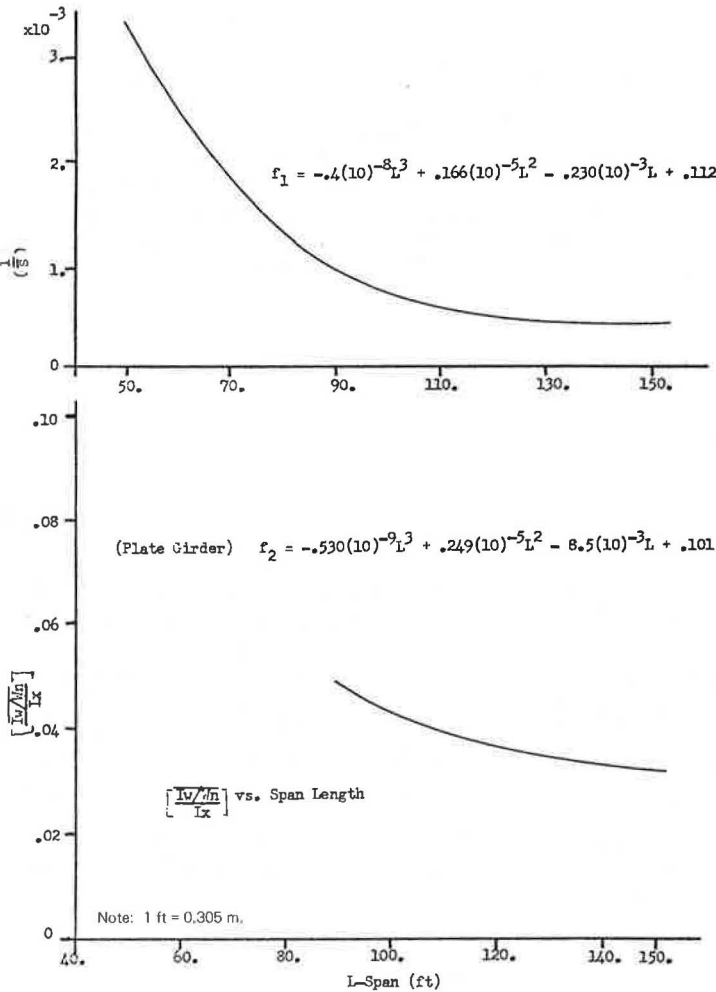
$$\text{Maximum bimoment}_{static} = 1.0(K_1 \times K_2 \times K_3) \tag{14}$$

6. Multiply maximum moment by $1 + I_f$ from equation 3, and multiply maximum bimoment by $1 + I_r$ from equation 4.

To account for S, one should multiply the resulting action of a single straight girder subjected to a line of truck wheels by $\overline{S}$. $\overline{S} = 1.29$ for S = 7 or 8 ft (2.14 or 2.44 m). $\overline{S} = 1.57$ for S = 9 or 10 ft (2.75 or 3.05 m).

Dead Load Design

The dead load response of curved bridge systems has been predicted by Murphy (4), and it realistically represents the response of the bare steel frame system. This technique has been computerized and then applied in the development of design curves. The curves represent maximum σ_b and σ_w as a function of R, L, I_x, and diaphragm S. The curves were based on typical girder properties obtained from a survey of bridge design as a function of girder length, as shown in Figure 3. If the actual design properties are different from the values in Figure 3, a correction factor is required to modify the chart values. Bending stress is related by the following:

$$\sigma_b = \overline{\sigma}_b C_1 \tag{15}$$

The warping stress is related by the following:

$$\sigma_w = \overline{\sigma}_w C_2 \tag{16}$$

The design charts, Figures 4 through 9, show the induced $\overline{\sigma}_b$s and $\overline{\sigma}_w$s normalized relative to the applied dead load per length. Thus any variation in dead load may be considered in an actual design. The normalized stress versus R/L values are plotted for span lengths of 100, 125, and 150 ft (30.5, 38.1, and 45.8 m). These plots are dependent on I_x, number of girders, and diaphragm spacing. The plots of $\frac{\overline{\sigma}_b}{W}$ versus R/L values (Figures 4, 6, and 8) are independent of diaphragm spacing and I_x, as determined in the development of the curves (4). The plots of $\frac{\sigma_w}{W}$ versus R/L values (Figures 5, 7, and 9) are dependent on diaphragm spacing and I_x. These curves are limited to a 4-girder system and are for specified stiffnesses. However, for other stiffness, the following equation may be applied:

$$\left(\frac{\overline{\sigma}_w}{W}\right)_e = \left(\frac{\overline{\sigma}_w}{W}\right)_{chart} \times \frac{\overline{I}_{rx}}{I_x} \tag{17}$$

where

$\left(\dfrac{\sigma_w}{W}\right)_e$ = referenced modified factor, and

$\overline{I}_{rx}$ = referenced chart value given in Figures 5, 7, and 9.

Figure 4. Normalized bending stress for a span length of 100 ft (30.5 m).
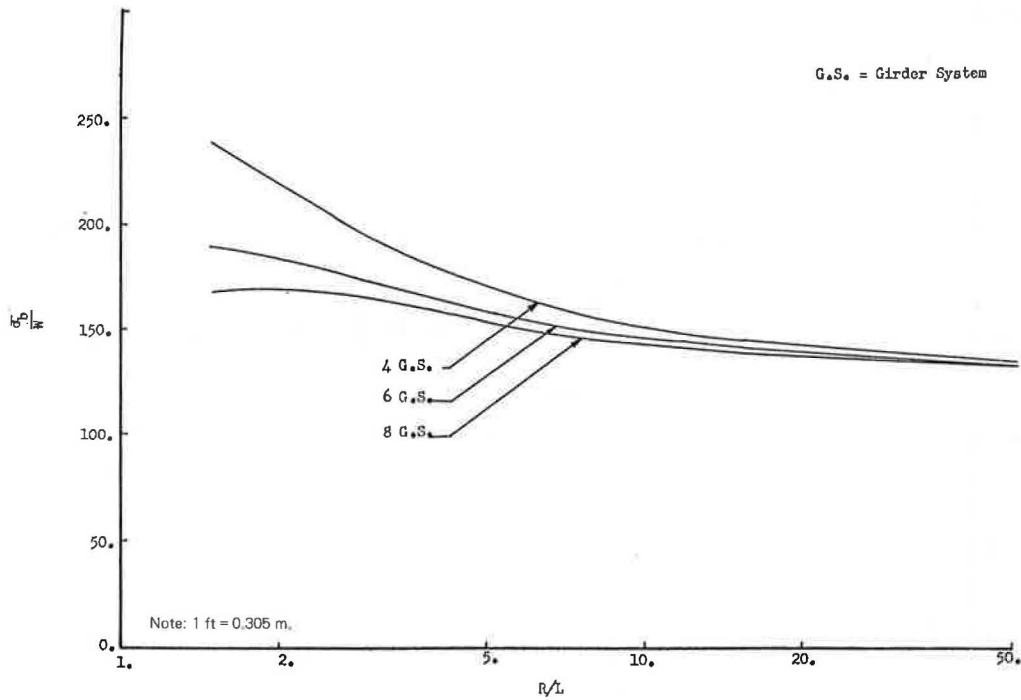

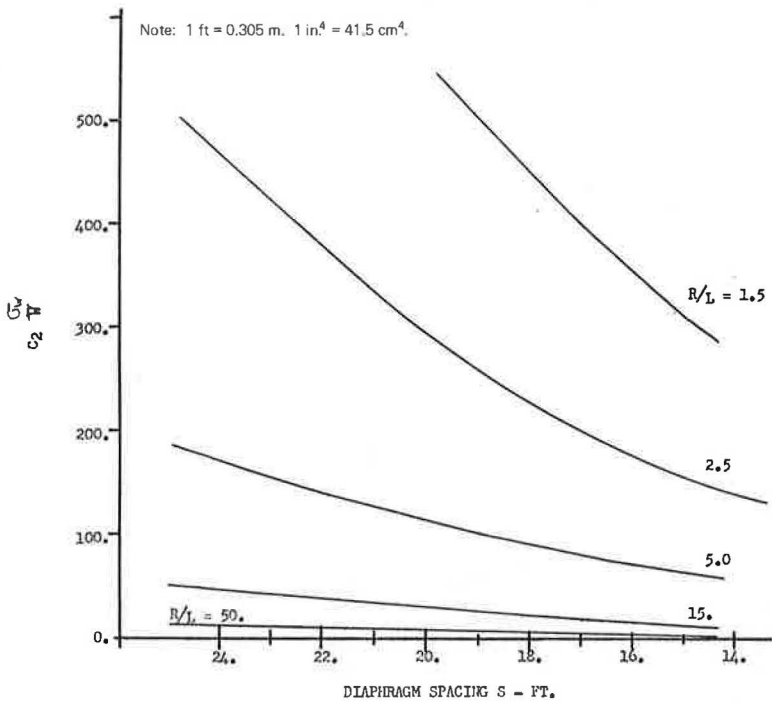Figure 5. Normalized warping stress for a span length of 100 ft (30.5 m).

Figure 6. Normalized bending stress for a span length of 125 ft (38.1 m).
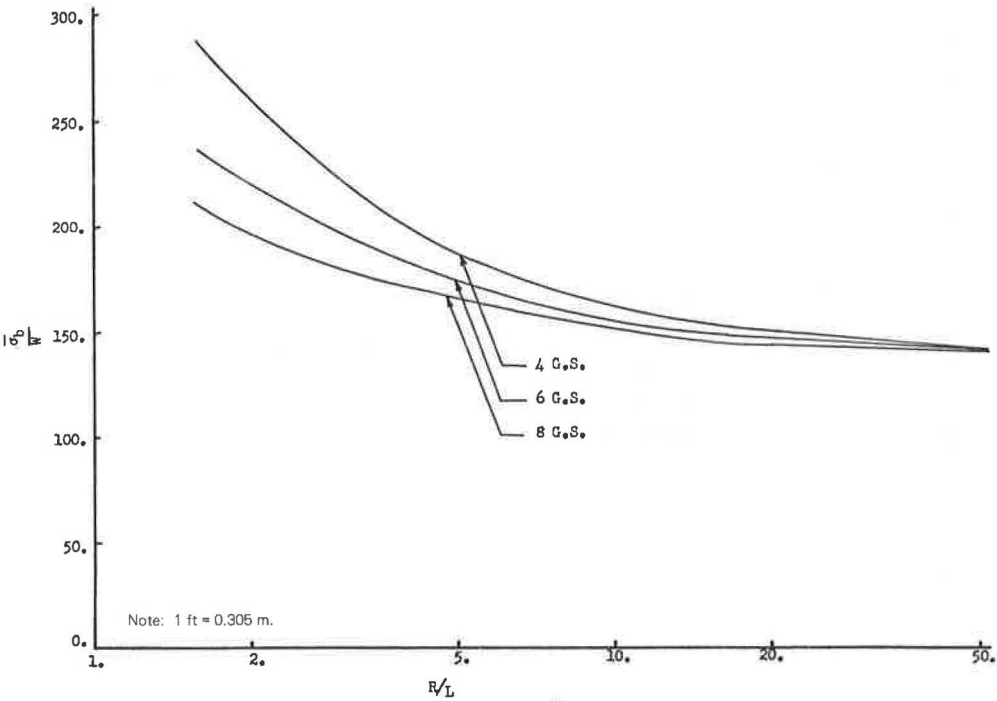

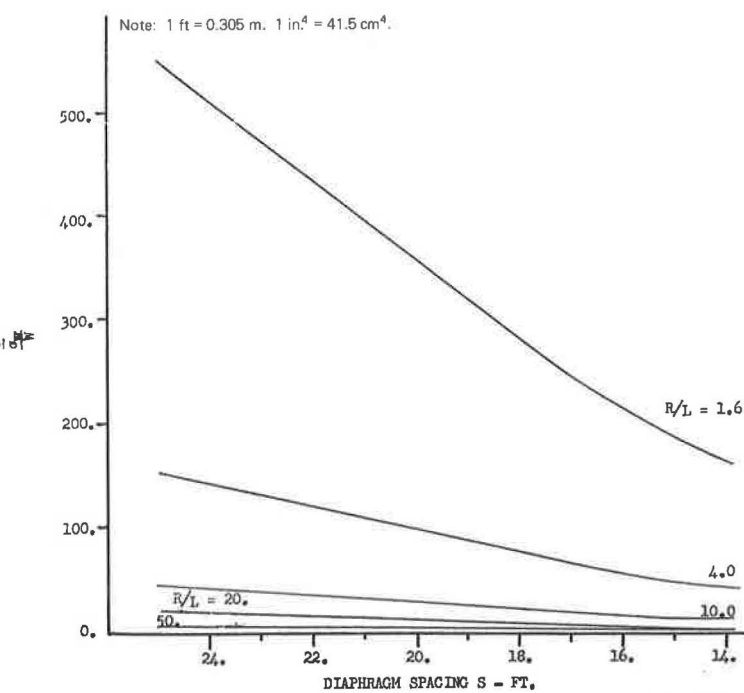Figure 7. Normalized warping stress for a span length of 125 ft (38.1 m).

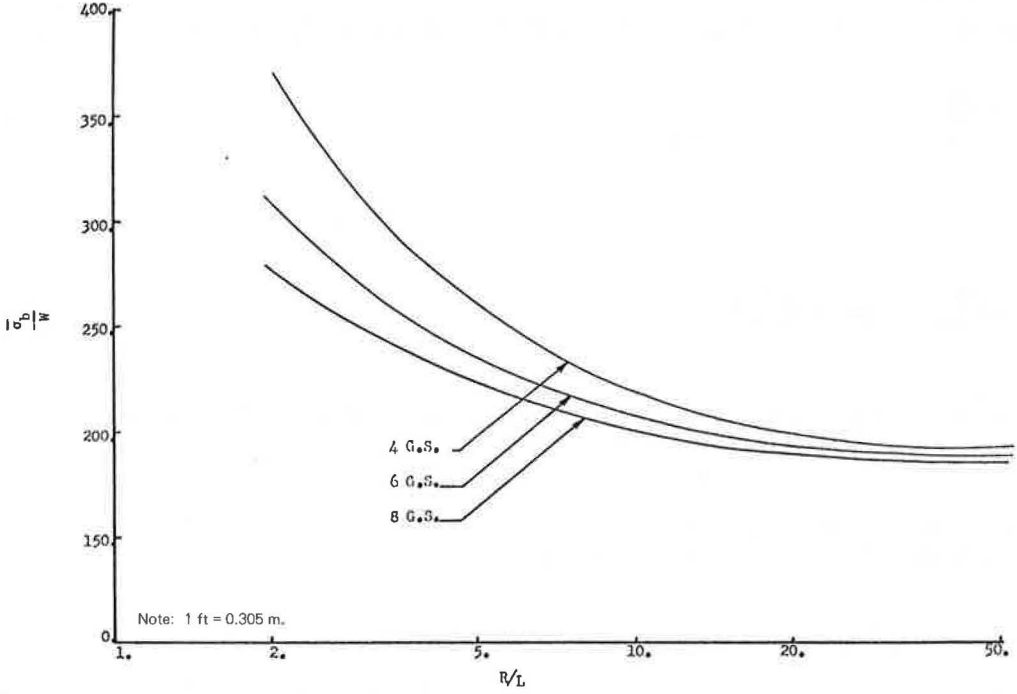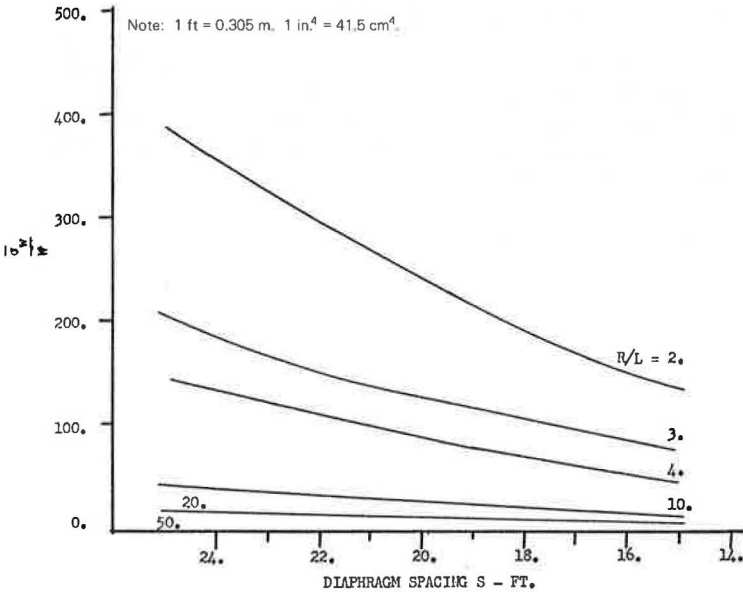**Figure 8. Normalized bending stress for a span length of 150 ft (45.8 m).**

Figure 9. Normalized warping stress for a span length of 150 ft (45.8 m).

14

To account for the behavior of 6- and 8-girder systems, one must modify the $\frac{\overline{\sigma}_x}{W}$ chart value. These chart values are modified by the following equation:

$$\left(\frac{\overline{\sigma}_x}{W}\right)_{exact} = \left(\frac{\overline{\sigma}_x}{W}\right)_{chart} - \Delta\left(\frac{\overline{\sigma}_x}{W}\right) \tag{18}$$

where

$$\Delta\left(\frac{\overline{\sigma}_x}{W}\right) = \frac{\overline{I}_x}{I_x} \frac{S^2}{(25)^2} \Delta\left(\frac{\overline{\sigma}_x}{W}\right)', \tag{19}$$

$\Delta\left(\frac{\overline{\sigma}_x}{W}\right)'$ = change in the value of the chart because of an increase in the number of girders beyond 4 girders shown in Figure 10, and

$\overline{I}_x$ = property given in Figure 10.

The curves were developed for a girder spacing of 8.0 ft (2.44 m). However, spacings up to 10 ft (3.05 m) are acceptable.

Torsional Properties

To determine design stresses or distortions, one must know girder section properties. If the girder is subjected to torsion and bending, the torsional properties, in addition to bending properties, will be required. The exact solution of the torsional properties of composite sections has been demonstrated (10). However, by idealizing the composite section, one can develop a series of simplified equations (11).

Figure 11 shows a typical composite girder and its pertinent dimensions. If we neglect the top girder flange and modify the concrete slab thickness, as shown in Figure 12, the dimensions are defined as follows: $t_1 = nt_s$, $d_1 = b_s$, $t_2 = W$, $d_2 = d_g + t_s/2 - t_f/2$, $d_3 = b_f$, and $t_3 = t_f$. Using these dimensions, one can determine the resulting torsional properties, which are shear center, normalized warping functions, warping stiffness, and torsional constant. Shear center is

$$\alpha = \frac{d_3^3 t_3}{(d_1^3 t_1 + d_3^3 t_3)} \, d_2 \tag{20}$$

Normalized warping functions are

$$W_{n_c} = \frac{\alpha d_1}{2} \tag{21}$$

for slab, and

$$W_{n_s} = \frac{(d_2 - \alpha)}{2} d_3 \tag{22}$$

for beam. Warping stiffness is

Figure 10. Normalized warping stress variation.

Note: 1 ft = 0.305 m. 1 in.^{4} = 41.5 cm^4.

$I_x = 32,000.$ in^4
$L = 100'$

$I_x = 80,000.$ in^4
$L = 125'$

$I_x = 125,000.$ in^4
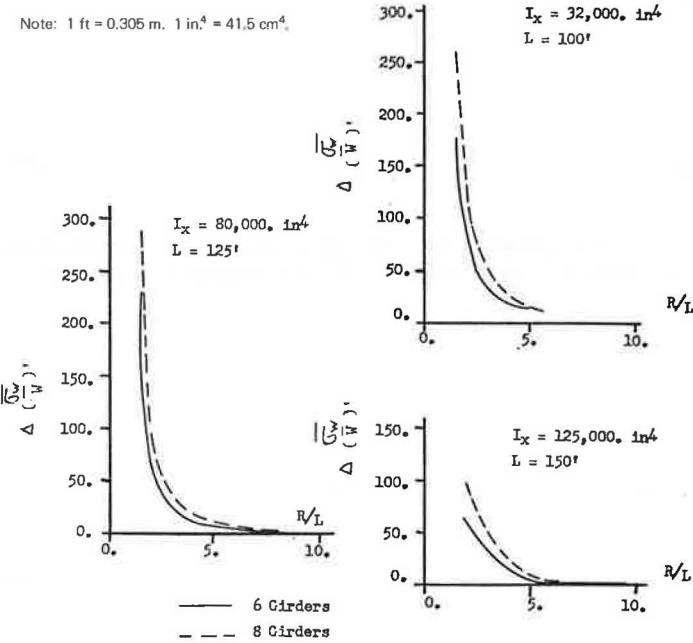$L = 150'$

——— 6 Girders
— — — 8 Girders
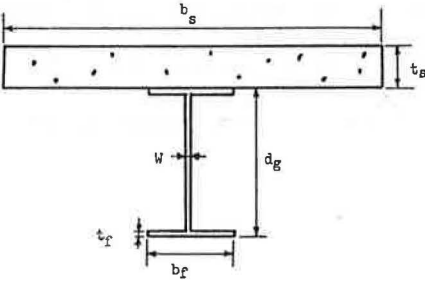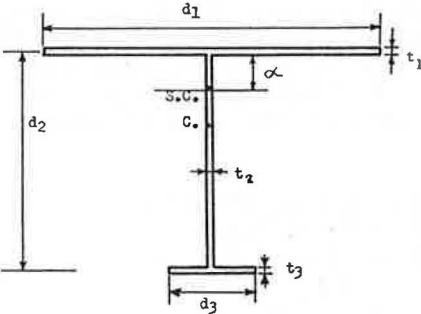
Figure 11. Typical composite section.

Figure 12. Idealized composite section.

$$I_{\ddot{n}} = \frac{\alpha^2}{12}\,t_1 d_1^3 + (d_n - \alpha)^2\,\frac{t_3 d_3^3}{12} \tag{23}$$

Torsional constant is

$$K_T = \frac{1}{3}(d_3 t_3^3 + d_2 t_2^3 + m d_1 t_s^3) \tag{24}$$

With the evaluation of these torsional properties, one can evaluate the resulting normal stresses in the composite section due to bimoment. Normal warping stress for slab is

$$\sigma_{W_c} = \frac{BiW_{n_c}}{I_w} \tag{25}$$

Normal warping stress for steel is

$$\sigma_{W_s} = \frac{BiW_{n_s}}{I_w} \tag{26}$$

DESIGN EXAMPLE

The design data just presented are sufficient to perform a preliminary design of a curved bridge system. Using these data, we will design a single-span, 4-girder bridge on which the girders are spaced 8 ft (2.44 m) apart at the centerline. Arc length is 98.0 ft (29.9 m); centerline radius is 588.8 ft (179.0 m). Slab thickness is 8.5 in. (21.6 cm), and the composite girder is made of A36 steel.

For live load effects, the following values, derived from the basic equations, are used:

1. $R_{cl} = 588.0$ ft (179.0 m),
2. $S = 8.0$ ft (2.44 m),
3. $L_{max} = 100.0$ ft (30.5 m),
4. $L_{cl} = 98.0$ ft (29.9 m),
5. $n = \dfrac{R_{cl}}{100} = \dfrac{588}{100} = 5.88$,
6. $M = \dfrac{L_{cl}}{50} = \dfrac{98}{50} = 1.96$,
7. $(L/R)_{cl} = \dfrac{98}{588} = 0.167$, and
8. $\bar{S} = 1.29\ (\underline{7})$.

The evaluation of K_1 from equations 6 and 7, gives

$$K_1 \text{ moment} = \frac{0.15}{n}(L/R) + 1$$

$$= \frac{0.15}{5.88}(0.167) + 1$$

$$= 1.004$$

K_1 bimoment $= [(35n)(L/R)^2 - 15(L/R)] \times 10^3$

$$= [(35 \times 5.88)(0.167)^2 - 15(0.167)] \times 10^3$$

$$= 3{,}250.$$

Evaluation of K_2 from equations 9, 10, and 11 gives

K_2 moment $= (n + 3)\left(\dfrac{0.4L}{R}\right) + 0.6$

$$= (5.88 + 3)(0.4 \times 0.167) + 0.6$$

$$= 1.194$$

K_2 bimoment $= \dfrac{(M - 1)}{6} (R/L)$

$$= \left(\dfrac{1.96 - 1}{6}\right)(6)$$

$$= 0.96$$

These values can be applied to the computed single straight girder moment, which was obtained from the loading of a single set of AASHO truck wheels on a 98.0-ft (29.9-m) girder.

$M_{straight} = (1{,}488.0 \text{ K}'/2 \times 12) \times \overline{S}$

$$= 744 \times 12 \times 1.29$$

$$= 11{,}500 \text{ kips/in. } (1300 \text{ kN/m})$$

$Bi = 1.0$

Applying equations 13 and 14, with $K_3 = 1.0$, one arrives at the following result for maximum forces in the 4-curved-girder system:

$M_b = 1.004 \times 1.194 \times 11{,}500 = 13{,}750 \text{ kips/in. } (1555 \text{ kN/m})$

$Bi = 3{,}250 \times 0.96 \times 1.0 = 3{,}120 \text{ kips/in.}^2 (21\ 528 \text{ MPa})$

Allowable design stress for A36 steel is 20 kips/in.^{2} (138 MPa). Assume that 35 percent of stress is due to live load, and 65 percent is due to dead load. Then

$$\sigma_b = 7 = \frac{M_b}{S}$$

$$S_{required} = \frac{13,750}{7} = 1,970 \text{ in.}^3 \text{ (32 200 cm}^3\text{)}$$

We will now study a composite section based on moment (10). The web is 60.0 by 0.375 in. (152 by 0.95 cm); the flanges are 16.0 by 1.5 in. (41 by 38 cm); and the slab is 8.5 by 96.0 in. (21.6 by 244 cm). The composite properties are as follows:

1. $I_x = 100,976.8$ in.^{4} $(42 \times 10^5$ cm^4),
2. $I_w = 2,255,951$ in.^{6} $(606 \times 10^6$ cm^6),
3. $S = 1,990$ in.^{3} (32 600 cm^3), and
4. $W_{n_c} = 527.4$ in.^{2} (3400 cm^2).

The steel girder properties are as follows:

1. $I_x = 51,949.0$ in.^{4} $(21.6 \times 10^5$ cm^4),
2. $I_w = 966,000$ in.^{6} $(261 \times 10^6$ cm^6),
3. $S = 1,650$ in.^{3} (27 100 cm^3), and
4. $W_{n_s} = 246$ in.^{2} (1590 cm^2).

Therefore, the induced live load stresses are

$$\sigma_b = \frac{M}{S} = \frac{13,750}{1,990} = 6.9 \text{ kips/in.}^2 \text{ (47.6 MPa)}$$

$$\sigma_w = \frac{BiW_n}{I_w} = \frac{3,120 \times 527.4}{2,255,951} = 0.73 \text{ kips/in.}^2 \text{ (5.05 MPa)}$$

Check dead load stresses from Figures 4 and 5. For a 4-girder system where L = 100.0 ft (30.5 m) and $(R/L)_{max} = \frac{600}{100} = 6.0$, then

$$\left(\frac{\overline{\sigma_b}}{w}\right) = 165$$

The dead load of the girder is computed as follows:

$$w = \frac{1}{12}\left\{[(60 \times 0.375) + 2(16 \times 1.5)]\frac{0.490}{144} + \left(\frac{8.5}{12} \times 8.0\right)0.150\right\}$$

$$w = 0.0875 \text{ kips/in. (1.53 kN/cm)}$$

Therefore,

$$\overline{\sigma}_b = 165 \times w$$

$$\overline{\sigma}_b = 165 \times 0.0875 = 14.4 \text{ kips/in.}^2 \text{ (100 MPa)}$$

Where $\overline{S}$ is the value given in Figure 3, the coefficient $C_1 = \overline{S}/S$. From Figure 3, when $L = 100.0$ ft (30.5 m)

$$1/\overline{S} = 0.9 \times 10^{-3}$$

$$\overline{S} = 1,111.1 \text{ in.}^3 \text{ (18 200 cm}^3\text{)}$$

Therefore,

$$C_1 = \overline{S}/S = \frac{1,111.1}{1,650}$$

$$C_1 = 0.673$$

Therefore,

$$\sigma_b = \overline{\sigma}_b C_1 = 14.4 \times 0.673$$

$$\overline{\sigma}_b = 9.65 \text{ kips/in.}^2 \text{ (66.5 MPa)}$$

The induced dead load warping stress is computed from Figure 5. If we assume a diaphragm spacing of 20.0 ft (6.1 m) and if $(R/L)_{max} = 6.0$, then

$$\left(\frac{\overline{\sigma}_w}{w}\right) = 100 \times \frac{\overline{I}_{rx}}{I_x}$$

$$\left(\frac{\overline{\sigma}_w}{w}\right) = 100 \times \frac{32,000}{51,949}$$

$$\left(\frac{\overline{\sigma}_w}{w}\right) = 61.9$$

$$(\overline{\sigma}_w) = 61.9 \times 0.0875$$

$$(\overline{\sigma}_w) = 5.4 \text{ kips/in.}^2 \text{ (37.3 MPa)}$$

The coefficient $C_2 = (Wn/Iw)/(\overline{Wn/Iw})$, where Wn/Iw is the design value and the $(\overline{Wn/Iw})$ value is found from Figure 3. If we use Figure 3 and if L = 100.0 ft (30.5 m), then $(\overline{Iw/Wn})/Ix = 0.044$ or $(\overline{Iw/Wn}) = 0.044 \times 51,949 = 2,280$. The design ratio is $(Iw/Wn) = \dfrac{966,000}{246} = 3,940$. Therefore,

$$C_2 = (Wn/Iw)/(\overline{Wn/Iw}) = \frac{2,280}{3,940} = 579$$

The warping stress is then equal to

$$\sigma_w = \overline{\sigma}_w C_2$$

$$\sigma_w = 5.4 \times 0.579 = 3.12 \text{ kips/in.}^2 \text{ (21.6 MPa)}$$

Total maximum normal stress is the sum of dead load and live load. The live load stresses, however, must include impact, which is found from Figures 1 and 2. This structure has an arc of $\theta = 9.5$ deg (use 15 deg). L = 98.0 ft (29.9 m), which gives $I_f = 0.19$, $I_T = 0.52$. The live load stresses are, therefore,

$$\sigma_b = 6.9(1.19) = 8.2 \text{ kips/in.}^2 \text{ (56.5 MPa)}$$

$$\sigma_w = 0.73(1.52) = 1.11 \text{ kips/in.}^2 \text{ (7.65 MPa)}$$

The combined dead and live load stresses are equal to the following (1 kip/in.^{2} = 6.9 MPa):

Load	Bending Stress (kips/in.^{2})	Warping Stress (kips/in.^{2})
Live	8.20	1.11
Dead	9.65	3.12
Σ	17.85	4.23

The combined bending and warping stress is $\sigma = 22.08$ kips/in.^{2} (153 MPa), which indicates that a new section might be selected. However, a computer system analysis using this selected stiffness and diaphragm spacing might be sufficient for an initial trial.

ACKNOWLEDGMENTS

REFERENCES

1. F. H. Lavelle and L. S. Boick. A Program to Analyze Curved Girder Bridges. Univ. of Rhode Island, Engineering Bulletin 8, 1965.
2. Highway Structures Design Handbook. United States Steel Corp., Vol. 1, 1967.
3. L. C. Bell and C. P. Heins. The Solution of Curved Bridge Systems Using the Slope-Deflection Fourier Series Method. Univ. of Maryland, Civil Engineering Rept. 30, June 1968.
4. E. L. Murphy and C. P. Heins. Dead Load Analysis of Single Span Curved Bridges. Univ. of Maryland, Civil Engineering Rept. 52, June 1973.
5. C. P. Heins. The Presentation of the Slope-Deflection Method for the Analysis of Curved Orthotropic Highway Bridges. Univ. of Maryland, Civil Engineering Rept. 15, June 1967.
6. K. R. Spates and C. P. Heins. The Analysis of Single Curved Girders With Various Loadings and Boundary Conditions. Univ. of Maryland, Civil Engineering Rept. 20, June 1968.
7. J. Siminou and C. P. Heins. Proposed Equations for Preliminary Design of Curved Girder Bridge Systems. Univ. of Maryland, Civil Engineering Rept. 25, June 1969.
8. K. M. Vashi and C. P. Heins. Impact Factors for Curved Highway Bridges. Univ. of Maryland, Civil Engineering Rept. 32, Sept. 1969.
9. L. C. Bell and C. P. Heins. Curved Girder Computer Manual. Univ. of Maryland, Civil Engineering Rept. 30, Sept. 1968.
10. J. T. C. Kuo and C. P. Heins. Torsional Properties of Composite Steel Bridge Members. Univ. of Maryland, Civil Engineering Rept. 37, June 1970.
11. J. T. C. Kuo and C. P. Heins. Behavior of Composite Beams Subjected to Torsion. Univ. of Maryland, Civil Engineering Rept. 39, Feb. 1971.

DISCUSSION

Douglas A. Nettleton, Federal Highway Administration

Charts are given in the paper for use in the design of curved I-girders, and a numerical example is worked out. The example consists of a simple span on a 588-ft (179.0-m) radius curve with an arc length of 98 ft (29.9 m), 4 girders spaced 8 ft (2.44 m) apart, and an 8.5-in.-thick (21.6-cm-thick) slab.

Dead load stresses are based on the assumption that 4 girders act with diaphragms spaced at 20 ft (6.1 m) and that the slab does not participate. Live load stresses are based on composite action of the slab and girders, but no account is taken of diaphragm spacing.

For live load, the slab is depended on for resistance to the rotational effect of curvature on the girder. It is implicitly assumed that the girder will retain its cross-section shape although the rotational and lateral restraining forces are applied at the top flange only. This assumed action requires the transmission of radial forces from the top flange to the bottom flange by means of the girder web. Such action would produce a bending of the web in a radial direction of such magnitude that the cross section of the girder would be distorted; stresses would be of a magnitude that could exceed the yield point. Properly spaced diaphragms would relieve the web of practically all of this stress and distortion, and the lateral bending or warping stress in the bottom flange would vary, approximately, with the square of the diaphragm spacing. By the method in this paper, no account is taken of diaphragm spacing in the determination of live load stress.

There is an error in the dead load calculation according to the values of $1/\overline{S}$ from Figure 3. This value should be about 0.75×10^{-3} instead of 0.9×10^{-3}. Use of the

corrected value changes the dead load bending stress from 9.65 kips/in.^{2} (66.6 MPa) to 11.6 kips/in.^{2} (80.0 MPa).

Live load impact was calculated as 19 percent for bending stress, and as 52 percent for warping or lateral bending stress. Because these stresses occur for the same loading at the same point and are additive, the calculations are a decided departure from past practice in design for impact.

Heins considers that failure to use diaphragms would be disastrous and that neglecting the direct effect of diaphragm spacing on live load lateral flange bending would seriously underestimate the lateral bending of the bottom flange.

AUTHOR'S CLOSURE

I appreciate Nettleton's comments and his observations concerning the effects of live load on the diaphragms. His last paragraph, however, implies that I suggested that no diaphragms were in the system during passage of the live load. This condition was neither implied nor stated. Influence of diaphragms on design is considered only under dead loading, but diaphragms are still present in the system during live load stresses. Although the thoughts given in this paragraph are interesting, they are not pertinent.

The graphs presented are for preliminary design. The value for $1/\overline{S}$ from Figure 3 given as 0.90×10^{-3} was rounded from 0.85×10^{-3}.

The impact values that were used were based on maximum effects as given in the curves. It was assumed that the worst case existed. Thus warping and bending stresses were added.

It should be realized, as I stated in the beginning of the paper, that the information presented is design data, which are helpful in selecting girder size and diaphragm spacings before computer analysis.

THERMAL STRESSES IN CONCRETE BRIDGE SUPERSTRUCTURES UNDER SUMMER CONDITIONS

M. Radolli and R. Green, Department of Civil Engineering,
University of Waterloo

Current design practice for deep concrete bridge superstructures generally ignores the influence of the diurnal heating cycle on the flexural response of members and, instead, considers mean temperature effects. A 1-dimensional heat-flow analysis is used to study the flexural deformations and stresses that are developed in deep concrete sections as a result of a typical summer heating cycle. Both nonlinear temperature and stress distributions are observed, and nonlinearity increases with member depth. An analysis of 2 typical continuous concrete structures indicates stresses exceeding those associated with live load and amounting to 40 percent of the allowable area possible for concrete structures having a depth of more than 4 ft (1.22 m).

•BRIDGE superstructures are affected by daily and seasonal temperature changes. These temperature changes cause longitudinal movement. In design of concrete superstructures, this movement together with creep and shrinkage is provided for with expansion joints (1). Little or no reference is made in design specifications to the effects resulting from temperature gradients through the depth of the bridge (2). The stresses resulting from these gradients appear to be closely related to the depth of the structure.

Concrete structures are being used more frequently for medium- and long-span bridges. The depth of these structures increases even though depth-to-span ratios may be nearly constant. Because of the increase in depth and because of the poor heat conductivity of concrete, temperature differentials between both upper and lower surfaces and interior and exterior of these deeper structures become considerably greater than those previously experienced for simple short-span structures.

Concern for predicting stresses that develop as a consequence of temperature gradients in deeper concrete structures is based on serviceability rather than strength. High local stresses can be induced during a temperature cycle of 12 h. For example, in a concrete structure, a free strain of 240 microstrains is possible on a hot summer day and easily might occur more than a thousand times during the life of the structure. This compares with the total shrinkage strain of 200 microstrains that is suggested in specifications (2). Local stresses caused by thermally induced strains frequently do not have the same sign as stresses induced by combinations of dead load, live load, and prestress (3).

Reynolds and Emanuel (1) have provided design engineers with a discussion of the most recent knowledge on thermal response of bridge structures. They have pointed out the need for further study of the prediction of thermal stresses. This paper discusses the form of both temperature gradients and stresses induced by these gradients in simple and continuous structures. Vertical temperature gradients can be nonlinear and result in nonlinear stress distributions. Such stress distributions frequently are not discussed in elementary texts. Analyses of several sections subjected to summer solar heating were carried out, and stresses exceeding live load stresses were predicted in a number of cases. A discussion of various field observations of bridge movements caused by temperature effects also is included in this paper.

TYPES OF THERMAL STRESS

The behavior of a structure as a result of the application of heat is different from its behavior caused by strain accompanied by stress, which results from load application. Strains do not induce stresses if the member is unrestrained when it is heated (Figures 1a and 1b). However, in fully restrained members stress occurs without strain (Figures 1d and 1e).

When a body is subjected to a nonuniform temperature gradient, irregular volume changes are produced. Thermal stresses arise because thermal expansion is restricted within the body. A similar body with a uniform or linear change in temperature undergoes free thermal expansion, and stresses are not developed.

As a consequence of a nonlinear temperature gradient, a set of self-equilibriating stresses develop throughout the depth of the section. These stresses result from induced internal strains developed to prevent the distortion of the plane section as a result of a nonlinear temperature distribution. Thus the nonlinear strain distribution caused by thermal effects plus a nonlinear strain distribution caused by the self-equilibriating stresses combine to satisfy the assumption of a total linear strain gradient. The self-equilibriating stresses are similar in form to the residual stresses present in rolled steel sections as a result of cooling and will be referred to as eigenstresses. Eigenstresses depend on the nonuniform deformation resulting from thermal effects and are independent of the boundary or support conditions of a structure.

If a simply supported beam under the influence of a nonuniform temperature gradient is allowed to deform freely (Figure 1c), then eigenstresses will be developed in the longitudinal direction. The beam also will assume an upward curvature. When the member is restrained, bending stresses are induced. This is shown in Figure 1d where axial expansion caused by an increase in mean temperature is allowed but where end rotation is restrained. The resulting bending stress adds to the eigenstress to give total thermal stress.

If the member is restrained axially (Figure 1e), then axial stress will be induced and mean temperature will change. Eigenstress, bending stress, and axial stress contribute to total longitudinal thermal stress in the member shown in Figure 1e where the ends are rigidly fixed.

Stresses arising from a restraint to axial or rotational movement are functions of the boundary conditions of the member. Eigenstresses are not a function of these boundary conditions but are directly related to vertical temperature distribution.

A summary of the effects of various vertical temperature gradients on both simply supported and continuous members is shown in Figure 1. Figure 1f illustrates the effect of a nonlinear vertical temperature gradient on the response of a 2-span continuous beam. Eigenstresses resulting from the nonlinear gradient are induced throughout the length of the beam. The gradient causes an upward positive curvature, and continuity stresses develop (3). The positive gradient shown is associated with summer daytime conditions. As a result of heating during a winter day, negative temperature gradients can develop as heat is lost from the surface of the structure during the evening. Figure 1f shows a typical summer daytime state. A winter state would be shown by reversing the stresses shown in the figure.

CONSEQUENCES OF THERMAL LOADING

In current bridge design practice, expansion devices are used to accommodate longitudinal thermal movements. Thermal stresses resulting from temperature gradients, however, generally are ignored. Observations indicate that thermal loading can seriously affect the serviceability as well as the structural integrity of a bridge structure (3, 4).

Hilton (5) has reported thermally induced vertical movements of simply supported steel bridge girders that have occurred before the concrete deck has been placed. An upward deflection of 0.40 in. (1 cm) was not uncommon on sunny days for a span length of 42.5 ft (13 m). A deflection of this magnitude can affect the final thickness of the

deck slab. Hilton (5) also found that the deflection of each girder was a function of its orientation to the sun and changed as the position of the sun changed.

Major stress-inducing effects caused by thermal loading occur in continuous structures. In a continuous bridge beam, a temperature rise at the upper surface produces positive flexural moments, which causes tensile stresses on the lower surface. Leonhardt and Lippoth (3) have reported crack damage caused by this type of thermal stress in 2-span continuous beams in the vicinity of the intermediate supports. This type of behavior and associated damage also have been observed in exposed building structures (6, 7).

A temperature difference between the top and bottom of a box-girder bridge also can result in thermally induced transverse bending and axial stresses (Figure 2) (4). With strong and prolonged solar radiation on the surface of a box-girder bridge, the interior air temperature increases and may exceed 100 F (38 C) (3). When the outer air cools during the night, a temperature difference between the interior and exterior of the box develops. For a temperature difference of 27 F (-2.8 C) between the outer and inner surfaces of a hollow box, transverse tensile stresses of 500 lb/in.^{2} (3500 kPa) are possible (3).

Damage to the abutments of an intermediate support line of a continuous, precast, prestressed bridge has been reported by Monnier (8). When heated, precast beams tend to "hog" upward (Figure 3) (8). If continuity reinforcement is absent at the bottom of the beams, horizontal prying forces that develop as a result of temperature change, creep, and shrinkage may cause damage (9, 10).

SOURCES OF HEAT

An exposed concrete bridge deck is heated or cooled by the following:

1. Convection to or from the surrounding atmosphere,
2. Radiation from the sun, and
3. Radiation to or from the sky or surrounding objects.

These sources are shown in Figure 4. Temperature changes induced by these sources depend on a number of factors such as:

1. Latitude of locality,
2. Orientation of bridge deck to the sun,
3. Time of day and season,
4. Degree of cloudiness and relative humidity,
5. Nature and color of bridge deck surface, and
6. Thermal properties of constituent materials of the bridge.

The maximum intensity of solar radiation occurs in the summer and generally increases with increasing proximity to the equator. Available data indicate a maximum intensity of incoming solar radiation on a horizontal surface between 11:00 a.m. and 2:00 p.m. (11, 12).

Radiant energy from the sun is partially reflected and partially absorbed. Reflected energy does not influence bridge temperature. Absorbed energy, however, heats the bridge deck surface and gives rise to a temperature gradient through the deck. Some of the absorbed radiant energy is lost from the surface by convection and reradiation (Figure 4). The radiation absorbed by a bridge deck is a function of the nature and color of the surface (absorptivity). A dark, rough surface has higher absorptivity than does a light, smooth surface and consequently absorbs more solar radiation.

The amount of radiant energy absorbed by the bridge deck from the atmosphere depends on the relative humidity of the air. This heat gain is often offset by the heat reradiated back into the atmosphere. Expressions for determining the heat radiated by and absorbed by a horizontal surface facing the sky are available (13).

Convective heat transfer from atmosphere to bridge deck is a function of wind

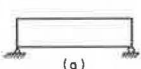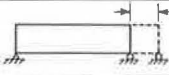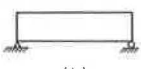**Figure 1. Effects of various temperature gradients.**
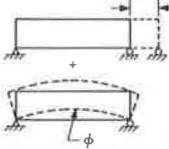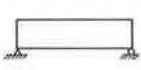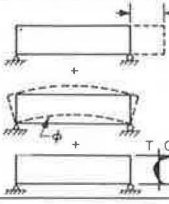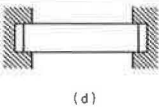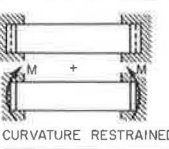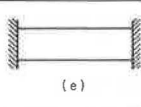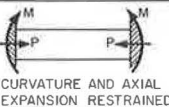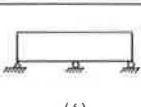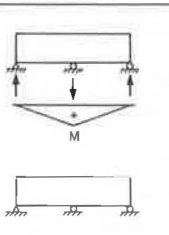
Figure 2. (a) Axial stresses caused by transverse elongation of deck slab and (b) bending stresses caused by restraint of transverse "hogging" in box girders.
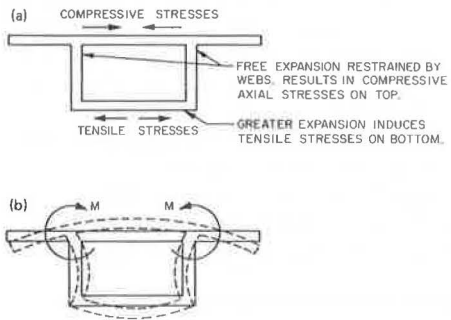
Figure 3. Support prying forces.
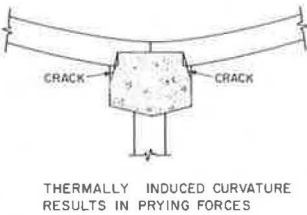
velocity, ambient air temperature, and deck surface temperature. The variation of both wind velocity and air temperature with time makes it difficult to predict heat gained by convection. By considering monthly average values of wind velocity and temperature, one can develop average values of heat transfer surface coefficients (14).

BRIDGE TEMPERATURES

Vertical temperature distribution through a concrete section depends on local weather conditions, section depth, and thermal properties of the concrete. The basic quantities that determine the thermal behavior of concrete are thermal conductivity, thermal diffusivity, specific heat, and coefficient of thermal expansion. These properties vary widely for typical concretes and are a function of composition of the mix, degree of saturation, and mineralogical character of the aggregate used (15, 16). An analysis of heat flow includes the following values for the concrete properties: 0.8 Btu·ft/ft². h·F (1.4 W/m·C), 0.02 ft²/h (0.002 m²/h), 0.23 Btu/lb·F (960 J/kg·C), and 6×10^{-6}/F (11×10^{-6}/C) for conductivity, diffusivity, specific heat, and coefficient of thermal expansion respectively. These values are typical for exposed concrete of normal weight.

Prediction of temperature effects on a structure from records of air temperature and solar radiation is important to design engineers. By interpreting regularly recorded weather data, they can make suitable provisions in design to resist or allow for movements and stresses induced by temperature changes. Both Barber (17) and Zuk (18) have been able to relate local weather data to maximum observed surface temperatures in bituminous and concrete pavements and bridge decks.

Analysis of temperature distribution throughout the depth of a section of a typical structure is complex because temperature varies with time, position in the section, and from section to section. Results to be presented are based on an analysis of 1-directional heat flow from the upper and lower surfaces of a unit strip taken from a wide beam or slab bridge deck. Included in the analysis are the following assumptions:

1. The member is homogeneous;
2. Surface heat transfer coefficients remain constant throughout the analysis time period; and
3. Thermal properties of the member are independent of temperature variation.

The 1-directional heat flow leads to a partial differential equation that was solved by using the finite difference method. The resulting iterative solution is similar to solutions developed by Emerson (19) and Krishnamurthy (20). When shade temperature, solar radiation, and wind at the exposed surfaces are known for a given day, then the temperature-time variation within a section can be obtained. Comparisons of measured and computed winter and summer gradients show good agreement (19). Because of the wide variation in climatic conditions in any given locality, a variety of temperature distributions is possible. Several such distributions have been observed or suggested on the basis of observed data. Included in these distributions are:

1. A linear temperature distribution in the top slab of a box section (21),
2. A constant temperature in the top slab of a box section (4), and
3. A distribution approximated by a sixth-degree parabola applicable to deep sections (4, 19).

The temperature distribution used in the third item has the form

$$t_y = \frac{Ty^6}{d^6} \tag{1}$$

where

    t_y = temperature at fiber in question,
    y = vertical distance from bottom of section to fiber in question,
    d = depth of section, and
    T = maximum temperature differential in the section.

A series of temperature distributions corresponding to the maximum temperature gradient was computed for rectangular concrete sections of different depths. The calculations were based on the values for conductivity, specific heat, and diffusivity previously mentioned. Values of solar radiation and ambient air temperature observed in Toronto, Ontario, on May 31, 1973, a day of high-intensity solar radiation and higher than average temperature range, were used in the analysis (Figure 5). Values of average solar radiation for the May to July period are similar for the United States and southern Canada. Hence the data shown in Figure 5 are representative.

The results of the analyses of the distributions are shown in Figure 6. It is apparent that temperature distribution is a function of section depth. For the shallowest section, temperature distribution is linear, and a temperature gradient of approximately 23 F (-5 C) exists. As section depth increases, surface temperature increases and appears to reach a maximum for sections greater than 30 in. (76 cm) in depth. Temperature distribution appears to be nonlinear for depths greater than 12 in. (30 cm), and temperature difference between upper and lower surfaces increases up to a section depth of 30 in. (76 cm) and remains constant for section depths greater than this. The central portion of the deeper sections does not appear to be affected by the diurnal heating cycle. A maximum temperature differential of 34 F (1.1 C) between the interior and the top surface appears to be typical for the deeper sections. Figure 6 also shows the temperature distribution corresponding to a sixth-degree parabola (equation 1). For sections greater than 24 in. (61 cm) deep the correlation between gradients calculated by using the heat transfer analysis and those predicted by a sixth-degree parabola is very good. However, for the 7-in. (18-cm) section, the correlation is poor.

Asphalt has a higher absorptivity than a normal gray-white concrete deck, and the surface temperature of a deck with asphalt will be different from that of a concrete deck without asphalt under similar climatic conditions. The computations were repeated for a concrete deck with a 2-in. (5-cm) asphalt covering. The temperature of the concrete below the asphalt was 6.3 F (-14.2 C) lower than that for an exposed deck. These results support the suggestion that a 1.5- to 2-in. (4- to 5-cm) thickness of surfacing is required before the insulation value of asphalt surfacing compensates for the greater heat absorption associated with dark surfaces (22).

In continuous structures, thermally induced curvatures result in continuity stresses. Maximum curvature occurs at the same time of day as maximum temperature gradient (12:00 noon to 1:00 p.m. for thin members and 3:00 p.m. to 4:00 p.m. for thicker sections). Thin sections developed larger curvatures than did thick sections (Figure 7). Continuity thermal stresses are a function of both curvature and member depth. The maximum continuity stress in a multispan continuous system is given by the following equation:

$$\sigma = C_1 C_2 E \phi d \qquad\qquad (2)$$

where

    σ = bending stress resulting from continuity,
    C_1 = a constant that is a function of number of spans (C_1 = 1.5 for 2-span system, C_1 = 1.0 for a multispan system)(3),
    C_2 = a constant that is a function of section geometry (C_2 = 0.5 for rectangular member),
    E = Young's modulus [taken as 5×10^6 lb/in.^{2} (34.5×10^6 kPa)],

Figure 4. Heat flow in exposed bridge deck.
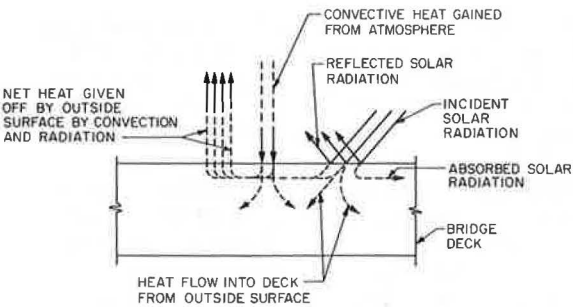
Figure 5. Intensity of solar radiation and range in ambient air temperature.
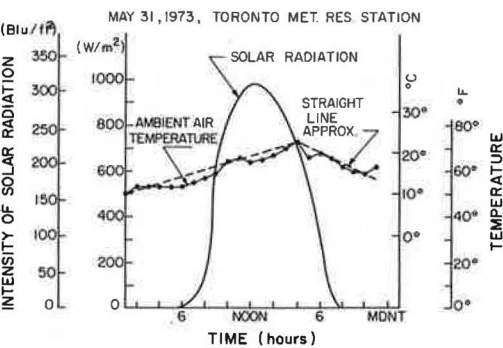
Figure 6. (a) Temperature distribution, (b) stress distribution corresponding to calculated gradient, and (c) stress distribution corresponding to sixth-order parabola for various section depths.

——————— CALCULATED GRADIENT

- - - - - - GRADIENT CORRESPONDING TO 6th ORDER PARABOLA

—·——·— INITIAL TEMPERATURE
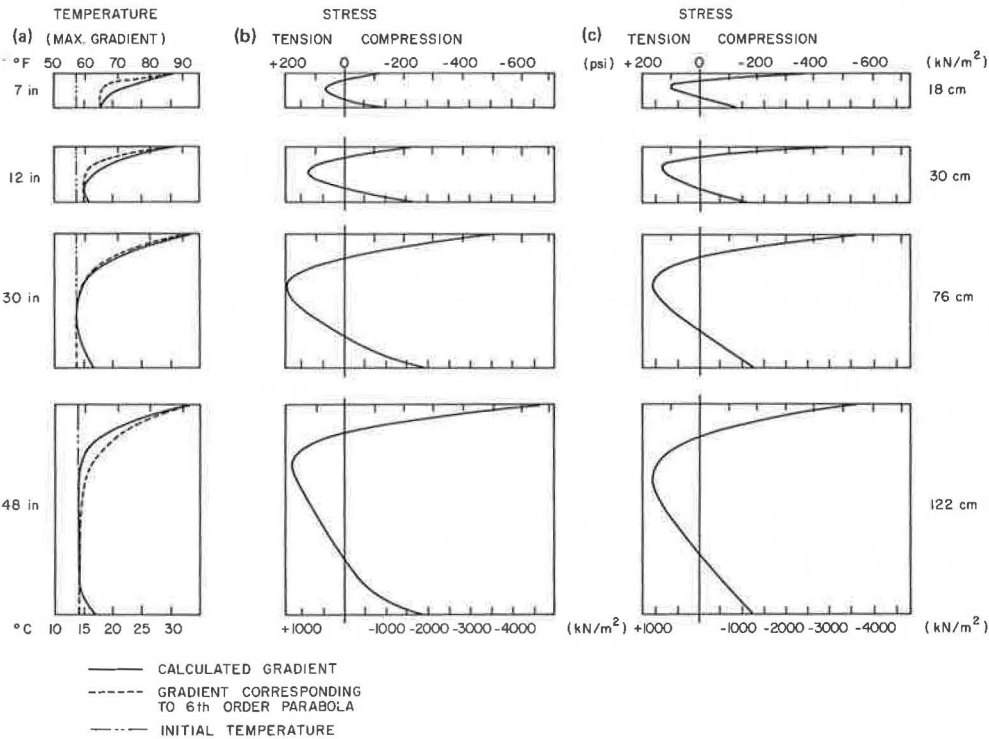
ϕ = curvature, and
$\dot{d}$ = member depth.

Thus continuity stresses are proportional to ϕd for a given material and span geometry. Figure 8 shows the relationship between nondimensional curvature and depth for both surfaced and unsurfaced members. The figure indicates that for rectangular members maximum continuity stresses occur in members that are approximately 15 in. (38 cm) deep. Figure 9 shows the influence of member depth on mean bridge temperatures for both surfaced and unsurfaced conditions. The difference between shallow and deep members exists because of the moderating influence of the interior of deeper slabs on temperature change. The computed maximum mean temperature and, therefore, maximum elongation occur between 6:00 p.m. and 7:00 p.m. for both shallow and deep slabs. This agrees with measurements of mean bridge temperature (19, 23).

Figure 10 shows the relationship between mean temperature and shade temperature for various depths. Mean temperature is higher than ambient shade temperature for sections thinner than 20 in. (51 cm). For thicker sections [>36 in. (92 cm)], the ratio of mean temperature to shade temperature appears to approach a constant value. Hence, if maximum shade temperature is known, mean temperature of a section of given depth under known climatic conditions can be estimated with reasonable accuracy.

THERMAL STRESSES

The analysis used in the prediction of stress is based on 1-dimensional beam theory and includes the following assumptions:

1. The material is homogeneous and isotropic;
2. Plane sections remain plane after bending is valid (Euler-Bernoulli assumption);
3. Temperature varies with depth, but transverse or longitudinal temperature variations do not exist;
4. Thermal stresses can be considered independently of stress or strain imposed by other loading conditions (principle of superposition applies); and
5. The section analyzed is far enough from a free end for end-distortion effects to be insignificant.

The resultant expression for longitudinal eigenstress, σ_z, at a distance above the neutral axis, has the following form (4, 23, 24):

$$\sigma_z = E\alpha \left[-\Delta T + x \frac{\displaystyle\int_{x_1}^{x_2} \overline{y}x\Delta T dx}{\displaystyle\int_{x_1}^{x_2} \overline{y}x^2 dx} + \frac{\displaystyle\int_{x_1}^{x_2} \overline{y}\Delta T dx}{\displaystyle\int_{x_1}^{x_2} \overline{y}dx} \right] \tag{3}$$

where

α = coefficient of thermal expansion,
x_1, x_2 = distance from neutral axis to extreme fibers,
$\overline{y}$ = total section width excluding voids,
x = distance from neutral axis to fiber in question,
ΔT = change in temperature, and
dx = thickness of elemental particle.

This expression applies to a long, thin member with no end restraints. If the second term in equation 3 is omitted, then the member has restraining moments at the ends

Figure 7. Maximum curvature versus depth.

Figure 8. Curvature × depth versus depth.

Figure 9. Maximum mean bridge temperature versus depth.

Figure 10. Ratio of mean temperature to shade temperature versus depth.

Figure 11. Maximum surface and interior stresses.

only. If the third term is omitted, then a restraining axial force only is present. If both the second and third terms are omitted, then the ends of the member are rigidly held.

Figure 6b shows the eigenstresses produced by the temperature gradients discussed previously. The stress distributions are character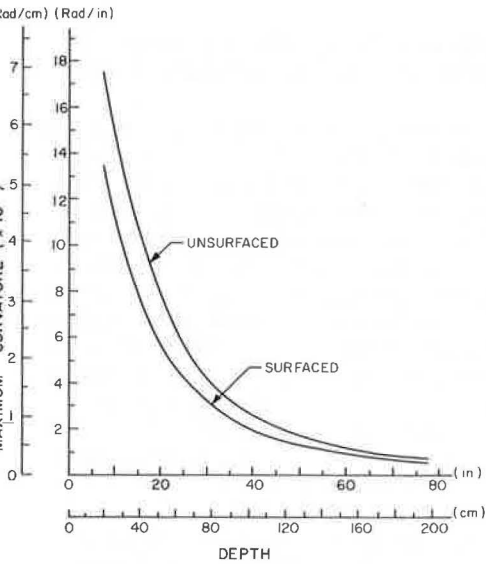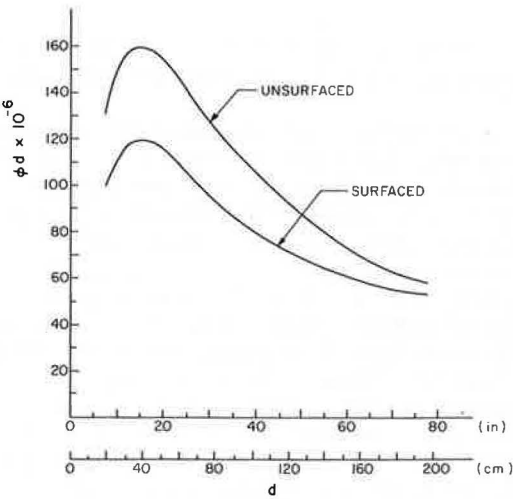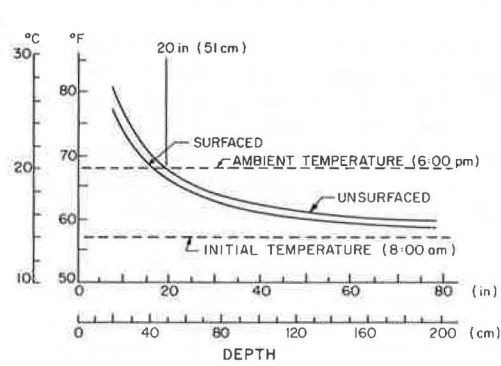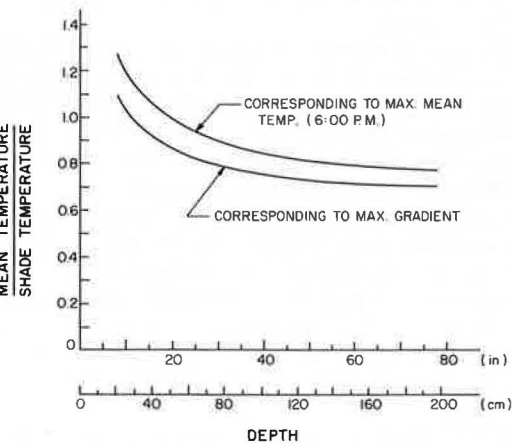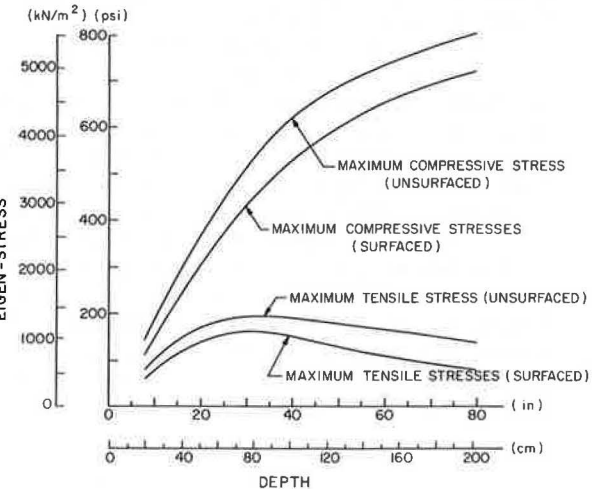istic of those produced by a positive temperature gradient. Compressive stresses are present in the upper and lower surfaces; tensile stresses are present in the central region of the section. As section depth increases, maximum compressive surface stress also increases; maximum interior tensile stress reaches a maximum at a depth of approximately 30 in. (76 cm). A summary of maximum stresses is shown in Figure 11 for both a surfaced and unsurfaced section. Adding 2 in. (5 cm) of asphalt lowers maximum stress levels slightly.

Stress values of more than 700-lb/in.^{2} (4800-kPa) compression were obtained on the top surface of some of the deeper sections. In prestressed members, where sustained compressive stress is present, the additional stress of 700 lb/in.^{2} (4800 kPa) corresponds to approximately 45 percent of an acceptable allowable stress [1,600 lb/in.^{2} (11 000 kPa)]. Combined longitudinal compressive stresses caused by live load, dead load, prestress, and thermal load reduce flexural tensile strength of concrete in the transverse direction (25).

A major stress-inducing effect of thermal loading in bridges occurs in continuous structures where interior supports offer restraint. To minimize the effects of dead load, many engineers construct new bridges that are cellular (that is, they include voided slabs, box girders, and T-beams). The magnitude of eigenstress is affected by web thickness in both box sections and T-sections. An increase in the ratio of web thickness to flange thickness results in an increase in maximum compressive stress and a decrease in maximum tensile stress (Figure 12). This trend is more pronounced in deep sections.

Figure 13 shows the influence of web thickness on induced curvature and indicates that curvature is insensitive to a change in web thickness. Similar results were obtained from various thermal stress analyses of T-sections with varying web thicknesses.

Although thermal stress caused by temperature gradients is generally ignored in design, Bosshart (26) has shown that stresses caused by thermal effects can be a large percentage of the total stress in continuous spans. Observations have indicated that, on a warm, sunny day, vertical temperature differences of 40 F (4.4 C) are possible. This temperature variation is considerably larger than variations specified in codes containing clauses dealing with temperature gradients (27). Temperature differences of this magnitude give rise to thermal stresses on the bottom fiber at a mid-span section that were equal in magnitude to maximum design live load stress and top fiber stresses that were 3 times as large as the stresses produced by maximum live load. Thermal stresses as high as 780 lb/in.^{2} (5400 kPa) were computed from observed temperature data (26).

Analysis of a continuous member under thermal gradient consists of predicting the magnitude of eigenstresses (equation 3) and continuity stresses (equation 2). For a given structure, one can use the data shown in Figures 7 and 12 to predict both continuity and eigenstresses.

Two typical, prestressed, concrete bridge structures were analyzed under thermal loading by using the solar radiation and ambient air temperature data shown in Figure 5. The structures chosen were a 2-span, prestressed, box-girder bridge with a section depth of 78 in. (198 cm) and a 3-span, prestressed, voided-slab bridge with a maximum depth of 52 in. (132 cm). The box-girder bridge is typical of box structures used in California. Typical stress values for dead and live load were available (28). The voided-slab bridge is representative of bridge structures used in Ontario. Values of stress caused by dead and live load were computed.

Eigenstresses for both box-girder and voided-slab bridges can be obtained from the data shown in Figure 12. Both the box-girder and voided-slab bridges were analyzed by considering equivalent I-sections, each of which had a different web thickness and depth. Induced curvature is insensitive to web thickness. Therefore, Figure 7, which is based on a rectangular section, can be used to obtain maximum curvature and continuity stresses.

Figure 12. Influence of web thickness on
eigenstress.
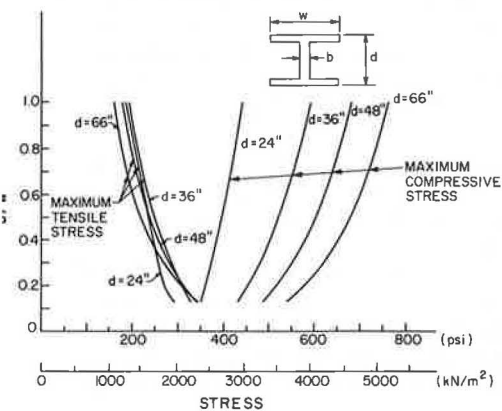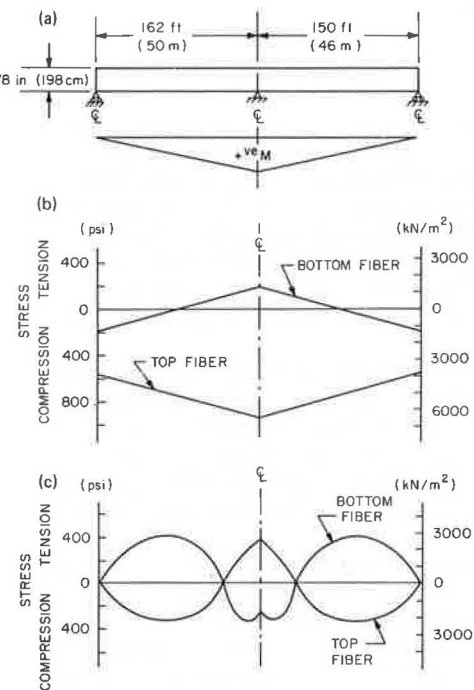
Figure 13. Influence of web thickness on curvature.

Figure 14. (a) Bending moment caused by thermal
load, (b) total thermal stress, and (c) live load and
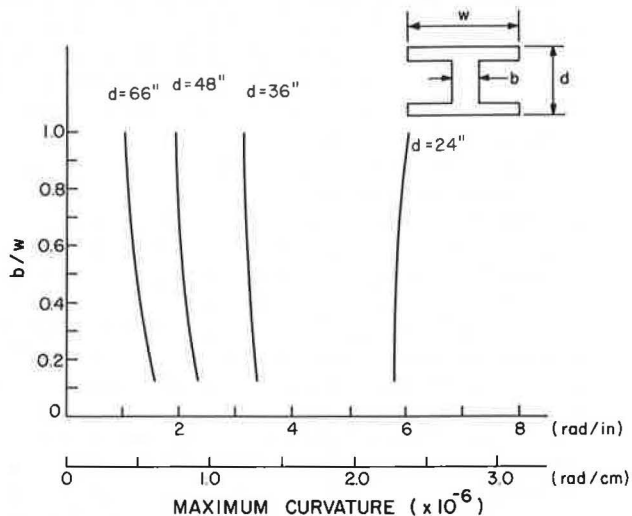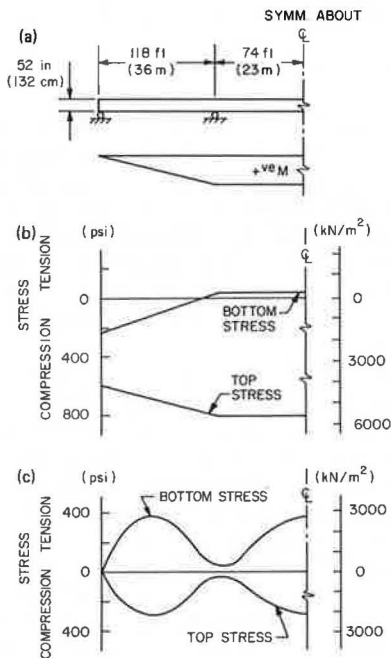impact stress in a box-girder bridge.

Figure 15. (a) Bending moment caused
by thermal load, (b) total thermal stress,
and (c) live load and impact stress in a
voided-slab bridge.

Figures 14 and 15 show the results of thermal stress analyses for the box-girder and the voided-slab bridges respectively. Figure 14b shows total thermal stress. Maximum thermally induced stress for the 2-span structure occurs on the top fiber at the intermediate support. Compressive stresses of 940 lb/in.^{2} (6500 kPa) are predicted. The entire top surface of the structure is in compression; average compressive stress is 770 lb/in.^{2} (5300 kPa), and this is due to thermal effects alone. Half of the bottom surface is subjected to tension; stresses are 200 lb/in.^{2} (1400 kPa) at the intermediate support.

Figure 14c shows the stresses caused by live load plus impact load. The stresses due to thermal effects are almost 2.5 times as large as those caused by live load plus impact at the mid-span section. They are greater than those caused by live load plus impact at every point on the top surface of the bridge.

The total design compressive stresses on the top surface are increased by 50 percent by the addition of thermal effects. This increase is from a maximum of 1,400 lb/in.^{2} (9700 kPa) to 2,100 lb/in.^{2} (14 500 kPa) at the mid-span sections. Stresses caused by thermal load, therefore, represent 33 percent of the total stress at the top fiber. At the bottom surface thermal stresses and stresses caused by gravity loads tend to cancel each other.

Figures 15b and 15c show respectively total thermal stress and live load plus impact stresses for the 3-span, voided-slab bridge. Top compressive stresses caused by thermal load are almost 3 times as large as those caused by maximum live load. Average compressive stresses of 715 lb/in.^{2} (4900 kPa) caused by thermal effects alone were obtained on the top surface; the entire center span was subjected to stresses of more than 800 lb/in.^{2} (5500 kPa). Bottom stresses were much smaller. Tensile stresses of only 40 lb/in.^{2} (280 kPa) were obtained on the bottom surface throughout the entire center span. Adding thermal stress increased total working top stress values by more than 47 percent. Total top fiber compressive stresses of more than 2,400 lb/in.^{2} (16 500 kPa) were obtained.

DISCUSSION OF FINDINGS

The strains introduced into concrete bridge structures as a result of a summer diurnal heating cycle are similar in magnitude to those associated with lifetime shrinkage strains. Similarly, stresses resulting from restraint of thermal strains can exceed those associated with design live load and can have a different sign. Solar heating or cooling introduces nonlinear temperature gradients in concrete structures. Hence expansion or contraction, which results from changes in the mean temperature, and bending, which develops as a consequence of the nonlinear gradient, should be considered in design. Current design practice appears to consider the influence of mean temperature only.

Analyses of rectangular, T-, and I-sections of various depths indicate that temperature distribution, stress distribution, maximum curvature, and maximum mean bridge temperature resulting from a typical diurnal heating cycle depend on section depth. Shallow sections generally exhibit larger curvatures and higher mean temperatures than deeper sections do. For deeper sections, the moderating influence of the interior where temperatures do not change appreciably during a daily heating cycle results in high self-equilibriating stresses and low curvature.

A detailed analysis of the stresses induced in various continuous concrete structures of various cross sections and depths indicates that surface compressive stresses of more than 900 lb/in.^{2} (6200 kPa) and interior tensile stresses of more than 300 lb/in.^{2} (2100 kPa) are possible on a typical hot summer day in a typical continuous concrete structure [48 in. (122 cm) in depth]. Local total thermal stresses several times larger than stresses caused by live load were computed. Consideration of thermal stress substantially increased (by 50 percent) total design stress and accounted for a third of total working stress. Typical reported thermal and elastic properties were assumed for the concrete in the 1-dimensional heat-flow analysis. The stresses previously noted show a sign change for winter conditions and have a magnitude of approximately 70 to 80 percent of the summer values.

The stresses developed as a consequence of heating and cooling cycles can affect the serviceability of concrete structures, particularly the deck slab in deep, solid-concrete structures and both deck slab and webs in cellular, box-type structures. The stress range caused by thermal effects plus gravity and prestressing loads and computed for 2 examples was found to exceed 40 percent of the allowable compressive design stress for these structures.

Thermal stresses caused by daily heating and cooling should be considered in conjunction with lifetime creep and shrinkage stresses and heat of hydration stresses. All these stress effects may contribute to the lack of serviceability of an exposed structure.

CONCLUSIONS

As a consequence of the relatively poor thermal conductivity of concrete, significant flexural stresses develop in concrete bridge superstructures when they are subjected to solar heating or cooling and changes in ambient temperature. These thermally induced flexural stresses can exceed 40 percent of the allowable compressive stress for concrete. Although they do not influence the strength of the superstructure, they can affect long-term serviceability.

Current design procedures should be considered adequate provided that reinforcing is well distributed throughout a concrete superstructure. Calculation procedures that consider stress-inducing thermal effects should be used to proportion the reinforcement.

ACKNOWLEDGMENTS

REFERENCES

1. J. C. Reynolds and J. H. Emanuel. Thermal Stresses and Movements in Bridges. Journal of Structural Division, Proc., American Society of Civil Engineers, Vol. 100, No. ST1, Jan. 1974, pp. 63-78.
2. Standard Specifications for Highway Bridges. American Association of State Highway Officials, 1973.
3. F. Leonhardt and W. Lippoth. Folgerungen aus Schaden an Spannbetonbrücken. Beton-und Stahlbetonbau, Heft 10, Vol. 65, Oct. 1970, pp. 231-244.
4. M. J. N. Priestley. Effects of Transverse Temperature Gradients on Bridges. Central Laboratories, New Zealand Ministry of Works, Rept. 394, Oct. 1971.
5. M. H. Hilton. Factors Affecting Girder Deflections During Bridge Deck Construction. Highway Research Record 400, 1972, pp. 55-68.
6. A. R. Meenan. Parking Garages for New Orleans Superdome. Journal of Prestressed Concrete Institute, Vol. 19, No. 2, March-April 1974, pp. 98-111.
7. J. N. Deserio. Thermal and Shrinkage Stresses—They Damage Structures! American Concrete Institute Publication SP27, 1971, pp. 43-49.
8. T. Monnier. Cases of Damage to Prestressed Concrete. HERON, Vol. 18, No. 2, 1972.
9. L. Zetlin, C. H. Thorton, and I. P. Lew. Design of Concrete Structures for Creep, Shrinkage and Temperature Changes. Symposium, Design of Concrete Structures for Creep, Shrinkage, and Temperature Changes, International Association for Bridge and Structural Engineering, Final Rept., Vol. 5, Zurich, Switzerland, 1970.
10. Handbook on the Unified Code for Structural Concrete. Cement and Concrete Association, London, England, CP110:1972, pp. 94-96.

36

11. F. H. Faust, L. Levine, and F. O. Urban. A Rational Heat Gain Method for the Determination of Air Conditioning Cooling Loads. Trans., American Society of Heating and Ventilating Engineers, Vol. 41, 1935.

12. Monthly Radiation Summary. Atmospheric Environment Service, Canada Ministry of the Environment, Information Canada, Ottawa, 1973.

13. J. S. Alford, J. E. Ryan, and F. O. Urban. Effect of Heat Storage and Variation in Outdoor Temperature and Solar Intensity on Heat Transfer Through Walls. Trans., American Society of Heating and Ventilating Engineers, Vol. 45, 1939, pp. 369-396.

14. M. W. R. Capps. The Thermal Behavior of the Beachley Viaduct/Wye Bridge. U. K. Road Research Laboratory, Crowthorne, Berkshire, England, Rept. LR234, 1968.

15. A. M. Neville. Properties of Concrete. Pitman Publishing Corp., New York, 1972, pp. 428-438.

16. D. G. R. Bonnel and F. C. Harper. The Thermal Expansion of Concrete. National Building Studies, Her Majesty's Stationery Office, London, England, Technical Paper 7, 1951.

17. E. S. Barber. Calculation of Maximum Pavement Temperature From Weather Reports. HRB Bulletin 168, 1957, pp. 1-8.

18. W. Zuk. Thermal Behavior of Composite Bridges—Insulated and Uninsulated. Highway Research Record 76, 1965, pp. 231-253.

19. M. Emerson. The Calculation of the Distribution of Temperature in Bridges. U. K. Transport and Road Research Laboratory, Crowthorne, Berkshire, England, Rept. LR561, 1973.

20. N. Krishnamurthy. Temperature Effects on Continuous Reinforced Concrete Bridge. Alabama Highway Department, Highway Planning and Research Rept. 58, Research Project 930-047, July 1971.

21. D. R. H. Maher. The Effects of Differential Temperature on Continuous Prestressed Concrete Bridges. Civil Engineering Transactions, Institution of Engineers, Australia, Vol. CE12, No. 1, Paper 273, April 1970, pp. 29-32.

22. A. W. Hendry and J. K. Page. Thermal Movements and Stresses in Concrete Slabs in Relation to Tropical Conditions. International Symposium on Concrete and Reinforced Concrete, Réunion Internationale des Laboratoires d'Essais et de Recherches sur les Materiaux et les Constructions, Part 2, July 1960, pp. 1-26.

23. W. I. J. Price and R. G. Tyler. Effect of Creep, Shrinkage and Temperature on Highway Bridges in the United Kingdom. Symposium, Design of Concrete Structures for Creep, Shrinkage, and Temperature Changes, International Association for Bridge and Structural Engineering, Final Rept., Vol. 6, Zurich, Switzerland, 1970, pp. 81-93.

24. R. Hoyle. Plane Strain and Plane Stress. In Thermal Stress, Sir Isaac Pitman and Sons Ltd., London, England, 1964, pp. 43-51.

25. G. Winter and A. H. Nilson. Design of Concrete Structures. McGraw-Hill Book Co., New York, 8th Ed., 1972.

26. H. Bosshart. Temperaturspannungen in Spannbetonbrücken. Symposium, Design of Concrete Structures for Creep, Shrinkage, and Temperature Changes, International Association for Bridge and Structural Engineering, Vol. 6, Zurich, Switzerland, 1970, pp. 73-80.

27. D. J. Lee. The Theory and Practice of Bearings and Expansion Joints for Bridges. Cement and Concrete Association, London, England, 1971.

28. Manual of Bridge Design Practice. California Department of Transportation, Section 7, 1971.

DIRECT METHOD FOR ESTIMATING PRESTRESS LOSSES

Ti Huang, Lehigh University

A rational method for estimating prestress losses in pretensioned concrete members is presented. The method is based on linking experimentally developed stress-strain-time relationships of steel and concrete materials. It enables a direct determination of stress and strain distributions in a member at any time within the service life of the member and avoids the need for step-by-step methods. Wide ranges of variation for concrete material characteristics and other design factors are permitted. The new method is illustrated by a practical design problem. Comparisons with 2 recently proposed procedures show good agreement of results.

•METHODS for estimating prestress losses in prestressed concrete members vary widely. At one time, a simple flat percentage or flat value was used in many design codes (1, 2). Today, complicated procedures involving the use of numerous equations, tables, charts, and a step-by-step method of calculation are required (3, 4). Neither extreme is satisfactory to the design engineers who want a simple, accurate, and flexible method that can accommodate variations in the numerous design and fabrication factors of prestressed concrete members.

This paper presents a rational method that permits a direct and accurate prediction of prestress losses throughout the service life of the member. Variations in material properties, geometrical design, and fabrication schedule are allowed for, and step-by-step calculations are avoided. In the present form, this new method applies only to pretensioned members, but the basic concept is equally valid for post-tensioned members.

In this paper, prestress is the stress in steel or concrete when all external loads, including the weight of the member, are temporarily and instantaneously removed. Consequently, the actual stress under a loaded condition is the sum of prestress and stress caused by all prevailing loads. Loss of prestress is due to the initial steel stress after anchorage. Therefore, prestress loss for a pretensioned member includes the effects of elastic shortening, shrinkage, creep, and relaxation. But friction and anchorage losses are not considered.

BASIC CONCEPT

The basic concept of the new method involves the use of stress-strain-time relationships to represent elastic as well as long-term rheological behavior of the steel and concrete materials. In the most general form, these relationships are given by the following equations:

$$f_s = f(\epsilon_s, t_s) = f_{s,e\ell} - f_{s,re\ell} \tag{1}$$

$$\epsilon_c = g(f_c, t_c) = \epsilon_{c,e\ell} + \epsilon_{c,sh} + \epsilon_{c,cr} \tag{2}$$

Equation 1 shows the steel tensile stress f_s as a function of steel strain ϵ_s and time after tensioning t_s, and as the difference between the elastic stress $f_{s,e\ell}$ and relaxation

---

loss $f_{s,rel}$. Equation 2 shows the concrete compressive strain ϵ_c as a function of concrete fiber stress f_c and time after end of curing t_o. It is the sum of elastic, shrinkage, and creep components. Here it is assumed that transfer of prestress occurs immediately after curing. Hence shrinkage and creep are controlled by the same time factor.

For a pretensioned concrete member, the stress-strain-time relationships of the concrete and steel materials are linked by the following 3 sets of linking conditions:

1. Time compatibility,

$$t_s - t_o = k_1 \tag{3}$$

2. Strain compatibility at the location of each prestressing strand,

$$\epsilon_s + \epsilon_c = k_2 \tag{4}$$

3. Equilibrium conditions over the cross section,

$$\int f_c dA_c - \Sigma f_s a_{ps} = P \tag{5}$$

$$\int f_c x dA_c - \Sigma f_s x a_{ps} = -M \tag{6}$$

where

$\quad k_1 =$ time interval from tensioning of steel to transfer of prestress (this includes
$\quad\quad$ time for form setting, casting, and curing),
$\quad k_2 =$ initial tensioning strain in steel,
$\quad A_c =$ area of net concrete section,
$\quad a_{ps} =$ area of individual prestressing element,
$\quad x =$ distance to elementary area from the centroidal horizontal axis,
$\quad P =$ thrust on section caused by external loads, and
$\quad M =$ bending moment on section caused by external loads.

The positive directions of x, P, and M are shown in Figure 1. In equations 5 and 6 the integrations are over the entire net concrete area, and the summations are over all pretensioning elements. All of the quantities defined for equations 3 to 6 are design or fabrication factors and are known or specified for the estimation of prestress losses. Thus equations 1 through 6 represent a set of 6 conditions for the 2 time variables t_s and t_c and the 4 stress and strain variables ϵ_s, ϵ_c, f_s, and f_c, which are functions of the location parameter x. A reasonable assumption was made that concrete stress varies linearly across the section

$$f_c = g_1 + g_2 x \tag{7}$$

When this condition is added, sufficient equations are available to evaluate all unknowns for any given time. That is, the time variations of stresses and strains can be determined. Thus, when the member design and the initial conditions k_1 and k_2 are known, a complete solution of the stress and strain distribution can be obtained by repeatedly solving equations 1 through 7 for different values of time. It is important to note that, for any specified time, solution is direct and not dependent on the solution at preceding times. Thus step-by-step accumulation is not needed. It also should by pointed out that f_s and f_c in the aforementioned equations include the effects of applied loads and, therefore, are not the prestresses as defined earlier. By definition, steel prestress and prestress loss are evaluated by the following equations:

$$f_p = f_s - f_{s\ell} \tag{8}$$

$$\Delta f_p = f_{s1} - f_p = f_{s1} - f_s + f_{s\ell} \tag{9}$$

where

   f_p = steel prestress,

   $f_{s\ell}$ = steel stress caused by applied loads including member weight and all permanent loads,

   Δf_p = loss of prestress, and

   f_{si} = initial steel stress immediately at anchorage.

STRESS-STRAIN-TIME RELATIONSHIPS

The functions f and g in equations 1 and 2 were developed experimentally based on observations of elastic, relaxation, creep, and shrinkage behavior of simple steel and concrete specimens. Steel relaxation data were obtained from strand specimens tested in fixed-length loading frames under various initial tensile stresses. To gather information on concrete strains, we used concentrically pretensioned rectangular concrete specimens in conjunction with similar specimens containing untensioned strands.

In selecting time functions for regression analyses of relaxation, shrinkage, and creep data, we placed special emphasis on the suitability of these functions for extrapolation because long-term projections based on short-term observations would be necessary. For this purpose, we made analyses by using data covering different periods of time and compared them with projected values for an arbitrarily chosen future time (100 years after tensioning). Lack of sensitivity of the projected final value to the amount of experimental data used in the analysis was used as a criterion in selecting time functions (5). A modified form of the logarithmic function was chosen because it was simple and because it satisfied the criterion of insensitivity.

Relaxation loss data from steel strand specimens were first analyzed for time and initial stress. The resulting expression then was combined with the elastic stress-strain relationship to form the stress-strain-time equation. The form of this equation is as follows:

$$f_s = f_{pu}\{A_1 + A_2\epsilon_s + A_3\epsilon_s^2$$

$$- [B_1 + B_2 \log (t_s + 1)]\epsilon_s - [B_3 + B_4 \log (t_s + 1)]\epsilon_s^2\} \tag{10}$$

where f_{pu} = specified ultimate tensile strength of steel in kips per square inch (megapascals). f_s is measured in kips per square inch (megapascals); ϵ_s is measured in units $\times 10^{-2}$; t_s is measured in days starting from initial tensioning.

The applicability of equation 10 is restricted because of the limited test ranges of the controlled factors. These ranges are

$$0.5 \leq f_s/f_{pu} \leq 0.8$$

$$1 \leq t_s \leq 36,500$$

The experimental work dealt with 270-kips/in.^{2}-grade (1860-MPa), stress-relieved, 7-wire strand specimens $^7/_{16}$ in. (1.11 cm) and $^1/_2$ in. (1.27 cm) in size. No significant size effect was found. The values of the regression coefficients are given in Table 1.

Equation 2 for concrete characteristics was developed in a similar manner by combining expressions representing elastic, shrinkage, and creep strains (6). Elastic strains were measure directly at the time of prestress transfer. The shrinkage strain of a prestressed member was defined to be the same as that of plain concrete containing no reinforcement. Creep strain was obtained from the measured total strain by deducting elastic-shrinkage and elastic-rebound strains. Time function for shrinkage and creep strains was selected by using the same criteria that were used for relaxation behavior. Coincidentally, the same function was chosen. The functional form of the concrete stress-strain relationship is as follows:

Figure 1. Sign convention for applied loads.
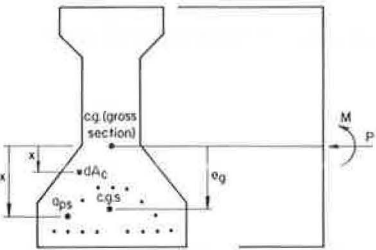
Table 1. Coefficients for steel stress-strain-time relationship.

Coefficient	Value	Coefficient	Value
Elastic		Relaxation	
A_1	-0.04229	B_1	-0.05867
A_2	1.21952	B_2	0.00023
A_3	-0.17827	B_3	0.11860
		B_4	0.04858

Note: All coefficients are dimensionless and are the same in SI units.

Table 2. Coefficients for concrete stress-strain-time relationship.

Coefficient	Value	
	Upper Bound Loss	Lower Bound Loss
Elastic strain, C_1	0.02500	0.02105
Shrinkage		
D_1	-0.00668	-0.00066
D_2	0.02454	0.01500
Creep		
E_1	-0.01280	-0.00664
E_2	0.00675	-0.00331
E_3	-0.00060	-0.00371
E_4	0.01609	0.01409

Note: C_1, E_3, and E_4 values will be combined with f_c. Multiply C_1, E_3, and E_4 values by 0.145 to convert to megapascals.

Figure 2. Example problem for predicted prestress losses.
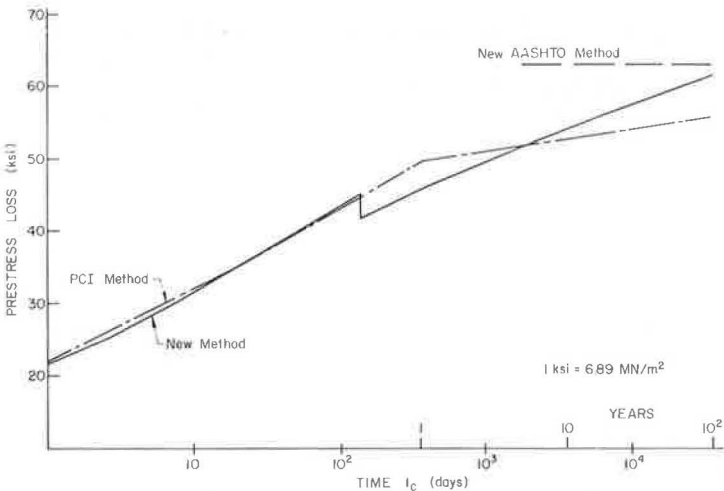
$$\epsilon_c = C_1 f_c$$
$$+ [D_1 + D_2 \log (t_c + 1)]$$
$$+ [E_1 + E_2 \log (t_c + 1)] + f_c [E_3 + E_4 \log (t_c + 1)] \tag{11}$$

ϵ_c is measured in units $\times 10^{-2}$; f_c is measured in kips per square inch (megapascals); and t_c is measured in days starting from the time of transfer, which is the same as the end of curing period.

In the experimental study, 2 concrete mixes were used, both of which satisfy the same minimum strength requirements [5.0 kips/in.^{2} (34.5 MPa) at transfer and 5.5 kips/in.^{2} (37.9 MPa) at 28 days]. However, their composition and manufacturing procedure were sufficiently different so that their rheological behaviors differed significantly. Two sets of regression coefficients were developed to reflect this wide variation. They are given in Table 2. The applicability of equation 11 is restricted because of the limited test ranges of the controlled factors. These ranges are

$$0 \le f_c \le 3.3 \text{ kips/in.}^2 \text{ (22.8 MPa)}$$

$$1 \le t_c \le 36,500$$

FORMULATION OF PROCEDURE

For any specified time, equation 10 reduces to a simple quadratic function of ϵ_s. Equation 11 is linear in terms of f_c. Their combination with equations 3 through 7 results in a pair of simultaneous quadratic equations in g_1 and g_2. The solution of g_1 and g_2 then enables one to evaluate steel and concrete stresses and strains over the entire cross section. Note that a general solution in this manner would result in different losses in the several prestressing elements and thus cause a gradual shift of the centroid of prestressing.

For practical purposes, all prestressing steel usually is regarded as concentrated at 1 point, the c.g.s., for stress calculations. When this simplification is used, the simultaneous quadratic equations can be simplified into a single quadratic equation in terms of the concrete fiber stress at c.g.s., f_{os}, as follows:

$$(R_1 - \beta f'_{c\ell}) + (R_2 + 1 - \beta)f_{cs} + R_3 f_{cs}^2 = 0 \tag{12}$$

where

f_{cs} = concrete fiber stress at c.g.s. in kips per square inch (megapascals),
  = $g_1 + g_2 e_s$,
$f'_{c\ell}$ = nominal concrete fiber stress at c.g.s. caused by applied loads in kips per square inch (megapascals),
  = $-\dfrac{P}{A_g} + \dfrac{M e_g}{I_g}$ (tension positive), and
β = dimensionless geometrical parameter.

β also can be represented as follows:

$$\beta = \frac{1}{A_{ps}\left(\dfrac{1}{A_g} + \dfrac{e_g^2}{I_g}\right)} = \frac{A_g I_g}{A_{ps}(I_g + A_g e_g^2)}$$

where

A_g = area of gross cross section in square inches (square centimeters),

I_g = moment of inertia of gross cross section in inches^4 (centimeters^4),

e_g = eccentricity of prestress for gross cross section in inches (centimeters), and

A_{ps} = total area of prestressing steel in square inches (square centimeters).

Equilibrium equations 5 and 6 also can be simplified to yield the value of steel stress at any arbitrary time:

$$f_s = (\beta - 1)f_{os} + \beta f'_{o\ell} \tag{13}$$

DERIVATIONS OF EQUATIONS

The set of equations used in the development of the basic analytical procedure includes the 2 stress-strain-time relationships (equations 10 and 11), the 4 linking relationships (equations 3 through 6), and the linear relationship defining concrete stress distribution in the member section (equation 7). In these equations, f_o, f_s, ϵ_o, and ϵ_s are functions of x. In equations 5 and 6, the integrations are over the net concrete section area, and the summations cover all prestressing steel elements. Substituting equation 7 into 5 and 6 and performing the integrations yields

$$A_g g_1 - \Sigma(f_s + f_{os})a_{ps} = P \tag{14}$$

$$I_g g_2 - \Sigma(f_s + f_{os})x_s a_{ps} = -M \tag{15}$$

where

f_{os} = concrete fiber stress at the level of prestress steel, and

x_s = x distance for an individual prestressing element.

Therefore,

$$f_{os} = g_1 + g_2 x_s \tag{16}$$

To simplify further derivation, we introduce a group of parameters.

$$P_1 = A_1 f_{pu}$$

$$P_2 = [A_2 - B_1 - B_2 \log(t_s + 1)]f_{pu}$$

$$P_3 = [A_3 - B_3 - B_4 \log(t_s + 1)]f_{pu}$$

$$Q_1 = D_1 + E_1 + (D_2 + E_2)\log(t_o + 1)$$

$$Q_2 = C_1 + E_3 + E_4 \log(t_c + 1)$$

Then,

$$f_s = P_1 + P_2\epsilon_s + P_3\epsilon_s^2 \tag{17}$$

$$\epsilon_c = Q_1 + Q_2 f_c \tag{18}$$

Substituting this information into equation 4 yields

$$\epsilon_s = k_2 - Q_1 - Q_2 f_{os} \tag{19}$$

Substituting this into equation 16 gives

$$f_s = P_1 + P_2(k_2 - Q_1 - Q_2 f_{cs}) + P_3(k_2 - Q_1 - Q_2 f_{cs})^2$$

$$= R_1 + R_2 f_{cs} + R_3 f_{cs}^2 \tag{20}$$

where

$$R_1 = P_1 + P_2(k_2 - Q_1) + P_3(k_2 - Q_1)^2,$$

$$R_2 = -Q_2[P_2 + 2P_3(k_2 - Q_1)], \text{ and}$$

$$R_3 = P_3 Q_2^2.$$

Substituting equations 16 and 20 into equilibrium condition equations 14 and 15 gives

$$A_g g_1 - \Sigma[R_1 + (R_2 + 1)(g_1 + g_2 x_s) + R_3(g_1 + g_2 x_s)^2] a_{ps} = P \tag{21}$$

$$I_g g_2 - \Sigma[R_1 + (R_2 + 1)(g_1 + g_2 x_s) + R_3(g_1 + g_2 x_s)] x_s a_{ps} = -M \tag{22}$$

These equations are simultaneous quadratic equations in g_1 and g_2.

In the simplified case when prestressing steel is regarded as concentrated at 1 level, x_s becomes a constant for all elements and is equal to e_g by definition.

Replacing x_s by e_g in equations 21, 22, and 19 gives

$$A_g g_1 - [R_1 + (R_2 + 1)(g_1 + g_2 e_g) + R_3(g_1 + g_2 e_g)^2] A_{ps} = P \tag{23}$$

$$I_g g_2 - [R_1 + (R_2 + 1)(g_1 + g_2 e_g) + R_3(g_1 + g_2 e_g)^2] A_{ps} e_g = -M \tag{24}$$

$$f_{cs} = g_1 + g_2 e_g \tag{25}$$

Multiply equation 23 by I_g and multiply equation 24 by $A_g e_g$; add these 2 equations and substitute equation 25. This gives

$$A_g I_g f_{cs} - [R_1 + (R_2 + 1)f_{cs} + R_3 f_{cs}^2] A_{ps}(I_g + A_g e_g^2) = PI_g - MA_g e_g$$

Therefore,

$$f_{cs} - [R_1 + (R_2 + 1)f_{cs}] A_{ps}\left(\frac{1}{A_g} + \frac{e_g^2}{I_g}\right) = \frac{P}{A_g} - \frac{Me_g}{I_g} \tag{26}$$

When we introduce

$$\beta = \frac{1}{A_{ps}\left(\dfrac{1}{A_g} + \dfrac{e_g^2}{I_g}\right)}$$

$$f'_{c\ell} = -\frac{P}{A_g} + \frac{Me_g}{I_g}$$

equation 26 is transformed into equation 12.

It is important to note that $f'_{c\ell}$ is the nominal concrete stress caused by the applied loads based on gross section properties. It uses a tension positive sign. The dimensionless geometrical factor β is associated closely with the ratio of steel prestress to concrete prestress.

Equation 13 for steel stress is obtained by subtracting equation 12 from equation 20.

ANALYSIS PROCEDURE

The procedure for an analysis of prestress losses in a pretensioned member is as follows when material, geometric, and fabrication factors, including the concrete characteristics β, f_c', k_1, and k_2, are known or specified for the problem:

1. Evaluate R_1, R_2, and R_3 for each specified time t_o;
2. Solve equation 12 for f_{os};
3. Evaluate the steel stress f_s by using equation 13;
4. Calculate concrete and steel strains ϵ_o and ϵ_s by using equations 2 and 4 respectively; and
5. Evaluate steel prestress and prestress loss by using equations 8 and 9 respectively.

EXAMPLE AND COMPARISON

This new method enables a direct solution of prestress loss at any time during the service life of the member without requiring a step-by-step accumulative technique. However, to determine the complete history of prestress variation in a member, the analysis procedure must be repeated many times for different values of t_o. The number of calculations involved is considerable. A computer program has been developed to carry out these calculations.

An example is presented here to illustrate calculations according to the new procedure and to compare the results with those from other procedures. This example deals with a Pennsylvania Department of Transportation standard 20/33 I-beam (2) that spans 60 ft (18.3 m) center to center. This beam is prestressed with thirty-four $\frac{1}{2}$-in. (1.27-cm) stress-relieved strands of the 270-kips/in.^{2} (1860-MPa) grade. The concrete used corresponds to the lower bound of prestress losses. e_g = 7.95 in. (20.2 cm); k_1 = 2.3 days; and f_{si} = 183.6 kips/in.^{2} (1266 MPa) = 0.68 f_{pu}. The beam is part of a highway bridge on which the deck slab is 7.5 in. (19.05 cm) thick and cast in place 140 days after transfer. The spacing between beams is 6 ft 10 in. (208 cm) center to center. An additional dead load of 30 lb/ft^2 (1440 N/m^2) is applied later to be resisted by the composite section.

For the sake of simplicity, the 30-lb/ft^2 (1440-N/m^2) superimposed load is treated as applied together with deck gravity load at 140 days. From the geometry of the given section, it is calculated that β = 50.5. Before application of superimposed loads, $f_{c\ell}'$ = 0.417 kips/in.^{2} (2.88 MPa) and $f_{s\ell}$ = 1.93 kips/in.^{2} (13.3 MPa). Afterwards, $f_{c\ell}'$ = 1.171 kips/in.^{2} (8.07 MPa) and $f_{s\ell}$ = 5.4 kips/in.^{2} (37.4 MPa).

Detailed calculations according to the new procedure are illustrated for the time just before the application of deck and other superimposed loads. At that time, t_o = 140 days, t_s = 142.3 days, $f_{c\ell}'$ = 0.417 kips/in.^{2} (2.88 MPa), and $f_{s\ell}$ = 1.93 kips/in.^{2} (13.3 MPa). The coefficients R_1, R_2, and R_3 in equation 12 will now be evaluated.

From the steel stress-strain relationship (coefficients A_1, A_2, and A_3 from Table 1) for the initial tensioning stress, f_{si} = 0.68 f_{pu} and k_2 = 0.65509.

$$P_1 = -0.04229 \ (270) = 11.4$$

$$P_2 = [1.21952 - (-0.05867) - 0.00023 \log (142.3 + 1)] \ (270) = 345.0$$

$$P_3 = [-0.17827 - 0.11860 - 0.04858 \log (142.3 + 1)] \ (270) = -108.4$$

$$Q_1 = -0.00066 - 0.00664 + (0.01500 - 0.00331) \log (140 + 1) = 0.0178$$

$$Q_2 = 0.02105 - 0.00371 + 0.01409 \log (140 + 1) = 0.0476$$

$$k_2 - Q_1 = 0.655 - 0.0178 = 0.637$$

$$R_1 = -11.4 + 345.0 \ (0.637) - 108.4 \ (0.637)^2 = 164.4$$

$$R_2 = -0.0476 [345.0 - 2(108.4)(0.637)] = -9.85$$

$$R_3 = -108.4(0.0476)^2 = -0.246$$

Substituting this into equation 12 gives

$$(164.4 - 50.5 \times 0.417) + (-9.85 - 49.5)f_{os} - 0.246 \ f_{cs}^2 = 0$$

or, more simply

$$143.3 - 59.3 \ f_{os} - 0.246 \ f_{cs}^2 = 0$$

The solution for f_{cs} is 2.39 kips/in.^{2} (16.5 MPa). From equation 13

$$f_s = 49.5 \ (2.39) + 50.5 \ (0.417) = 139.5 \ \text{kips/in.}^2 \ (962.5 \ \text{MPa})$$

Hence

$$f_p = 139.5 - 1.93 = 137.6 \ \text{kips/in.}^2 \ (959.4 \ \text{MPa})$$

$$\Delta f_p = 183.6 - 137.6 = 46.0 \ \text{kips/in.}^2 \ (317 \ \text{MPa})$$

It should be reemphasized that prestress loss is calculated directly from initial and present conditions without any reference to intervening loading history. Figure 2 shows the computer results of similar calculations at other times.

From Figure 2, it is easily seen that the growth of prestress loss is nearly linear with respect to log t_c as long as the load remains unchanged. It would be reasonable, therefore, to simplify the calculating procedure by taking advantage of this phenomenon. Direct solution will be needed only at a few key stages, and prestress loss at an intermediate time can be estimated easily by means of this linear semilogarithmic relationship.

Figure 2 also shows estimates based on a step-by-step procedure recommended by the Prestressed Concrete Institute (PCI) (4) and by a procedure of the American Association of State Highway and Transportation Officals (AASHTO) (8). Calculation according to a 1973 specification (7) resulted in an extremely high loss estimate of nearly 80 kips/in.^{2} (552 MPa) and was not shown in Figure 2. Two of these methods appear to have implicitly defined prestress to include the stress caused by applied loads (4, 8). For the comparison to be meaningful, all estimates shown in Figure 2 have been adjusted to conform to the definition for prestress given in this paper.

Very good agreement is noted between the PCI method (4) and the new method presented in this paper, particularly during the initial period before the increase of external load. The low estimate of the final loss by the PCI method [55.5 kips/in.^{2} (383 MPa)] is believed to be a reflection of a relatively short assumed service life.

The AASHTO method (8) deals with the final loss only and does not yield as much information as the other 2 methods do. Although the final loss predicted by the AASHTO method [62.6 kips/in.^{2} (432 MPa)] appears to agree quite well with the prediction by the new method [61.1 kips/in.^{2} (421 MPa)], there are indications that AASHTO also considered a service life shorter than 100 years. Consequently, it would be more appropriate to recognize the difference and conclude that the AASHTO method results in slightly higher loss predictions than the new method does. It should be reiterated that, in this example, concrete corresponding to lower bound losses is considered. The new method is very sensitive to the characteristics of concrete, but the AASHTO method is not. In the AASHTO method, only the elastic loss is affected. When the same example was repeated using high-loss concrete, the new method yielded a final loss of 76.9 kips/in.^{2} (530 MPa) at 100 years; the AASHTO method resulted in a significantly lower loss of only 65.4 kips/in.^{2} (451 MPa) at an unspecified time. Similar comparisons have been observed in other examples. In general, it can be stated that the AASHTO procedure yields predicted final loss values lying within the range predicted

by the new method, but they are much closer to the lower bound.

CONCLUSION

The new method for estimating prestress losses is a workable alternative to the several methods currently available. It allows for wide ranges of variation in material characteristics and other design factors, and it enables the direct determination of prestress loss at any time during the service life of the member.

ACKNOWLEDGMENT

REFERENCES

1. Standard Specifications for Highway Bridges. American Association of State Highway Officials, 10th Ed., 1969.
2. Standards for Prestressed Concrete Bridges. Pennsylvania Department of Transportation, Forms ST202 to ST208, 1964.
3. International Recommendations for the Design and Construction of Concrete Structures. European Commission on Concrete, 1970.
4. Tentative Recommendation for Estimating Prestress Losses. Committee on Prestress Losses, Prestressed Concrete Institute, final draft, Sept. 1973.
5. E. G. Schultchen, H. T. Ying, and T. Huang. Relaxation Behavior of Prestressing Strands. Lehigh Univ., Fritz Laboratory Rept. 339.6, March 1972.
6. H. T. Ying, E. G. Schultchen, and T. Huang. Estimation of Concrete Strains and Prestress Losses in Pretensioned Members. Lehigh Univ., Fritz Laboratory Rept. 339.7, May 1972.
7. Standard Specification for Highway Bridges. American Association of State Highway Officials, 11th Ed., 1973.
8. Proposed Revision to Standard Specification for Highway Bridges, Article 1.6.7. Committee on Structures and Bridges, American Association of State Highway and Transportation Officials, 1974.
9. T. Huang. Prestress Losses in Pretensioned Concrete Structural Members. Lehigh Univ., Fritz Laboratory Rept. 339.9, Aug. 1973.

FIELD TESTS OF A STEEL-COMPOSITE BOX-GIRDER BRIDGE

Raymond E. Davis, Division of Structures,
  California Department of Transportation, and
Gary A. Castleton,* Santa Clara County Government, California

Field tests were performed to assess the behavior of a steel box-girder bridge with a composite-concrete roadway deck slab. The structure was instrumented at a mid-span cross section and at a section near the support of 1 of the simple approach spans to permit studies of bending and shear strain distributions. Live load was applied, and theoretical analyses were performed with a finite element program. Live load membrane strains can be accurately predicted by the program, but fiber strains, especially in the transverse direction, are greatly influenced by plate warpage and initial local dead load deflections. Observed dead load strains exhibit significantly greater shear lag than that predicted by the program. Live load and ultimate dead load deflections are closely approximated by the theoretical analysis. The program overestimated the torsional stiffness of both the bare steel girder and the composite section. Success of the finite element program in assessing structural behavior of the steel box girder coupled with previously demonstrated deficiencies in methods of design employing distribution factors provides a convincing argument for using such a program in future designs of this type of structure.

•TESTS were performed by the California Department of Transportation on a steel box-girder bridge with roadway slab of composite concrete to study structural behavior and assess the validity of a computerized finite element analysis for predicting strains and deflections of the structure (1).

FIELD TESTING

Description of Prototype

The prototype is a twin structure that is 4,050 ft (1234 m) long and crosses the Sacramento River at Bryte Bend on I-880. The test span is the twentieth simple span of the right structure. It is a 146.5-ft (44.7-m) span with a uniform cross section between supports as shown in Figure 1.

The structure was designed on the basis of gross moment of inertia. Secondary effects of torsion were considered. It was assumed that 4.5 lanes were loaded with AASHTO design loads. These loads were distributed transversely, and we assumed that a simple beam distribution existed between webs.

48

Instrumentation

The structure was instrumented at a primary plane near mid-span as shown in Figure
2. A secondary plane near a support was instrumented with a small number of SR-4
rosette transducers on each of the webs.

Housed in an instrumentation trailer beneath the span was the major item of elec-
tronic readout hardware: a computer-controlled, high-speed, multiplexing, data-
acquisition system capable of scanning up to 100 transducer circuits at 5,000 readings/s.
Thus when a test vehicle traversed the span at crawl speeds of 3 ft (1 m)/s, each of 100
circuits in the system was scanned for each $\frac{3}{4}$ in. (19 mm) of vehicle travel.

Test Vehicles

Two vehicles were employed in the research. One was the FHWA 1959 Autocar, the
dimensions of which approximate those of the standard AASHTO HS20 truck. The other
was a 7-axle, double-goose-neck, low-bed hauler. The simulated AASHTO vehicle was
ballasted with reinforcing bar ingots to a gross load of 75,000 lb (34 000 kg); the 7-axle
vehicle was ballasted to 220,000 lb (100 000 kg).

The simulated AASHTO vehicle could produce a maximum bending moment of 2,300
kip·ft (3100 kN·m), which is about 20 percent of the 11,000 kip·ft (14 900 kN·m) design
moment for live load plus impact. The heavier vehicle produced a total moment of
5,900 kip·ft (8000 kN·m). A profile drawing of the heavier vehicle is shown in Figure 3.
This figure also shows measured 4-wheel axle reactions. Longitudinal runs were made
in 16 transverse locations on the roadway at approximately 2-ft (0.6-m) intervals.

Data Acquisition and Processing

Road switches placed on the deck at the eighth points of the span provided a means of
accurately locating each axle at any time. Of the 370,000 items of data recorded on
magnetic tape during each crossing, 10 readings/transducer circuit were read and
averaged by a data processing program. Transverse distribution of transverse and
longitudinal strains was plotted for various transverse vehicle positions.

THEORETICAL ANALYSES

Finite Element Program

Analyses of the structure by means of a computerized finite element code (FINPLA)
were employed in comprehensive studies of observed strain patterns (2, 3). This
program is especially fitted to this type of structure because most of the structural
elements including the steel plates, steel flanges, concrete slab, transverse and longi-
tudinal ribs (stiffeners), cross-frame members, and diaphragms can be mathematically
modeled. The program employs a rectangular finite element with 24 degrees of free-
dom; 6 are at each node. Membrane actions are described by 2 in-plane displacements
and a rotation about a normal to the plane of the element at each node. Slab actions
are described by 2 rotations about in-plane axes and a displacement normal to the plane
of the plate at each node.

Structure Separation

The tested span was separated by 34 longitudinal blocks of 33 elements, each of which
was bounded by transverse and longitudinal stiffeners. The steel flanges of the box
were idealized as longitudinal stiffeners because they were some distance below the

Figure 1. Cross section of prototype.
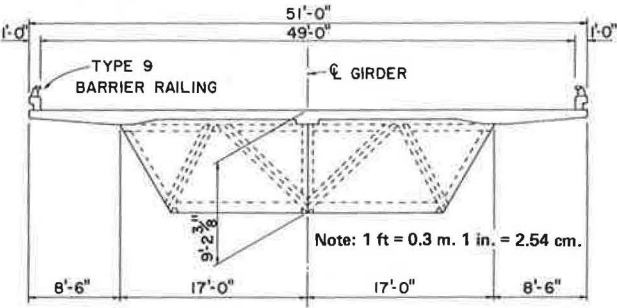
Figure 2. Prototype half cross section showing instrumentation at mid-span.

SYMBOL	TYPE OF TRANSDUCER
⊗	CARLSON STRAINMETER
L	SR-4 CROSS GAUGE
↗	SR-4 ROSETTE GAUGE
• or —	SR-4 SINGLE GAUGE
↓	DEFLECTOMETER
(DC)	SR-4 DUMMY GAUGE (Conc.)
(DS)	SR-4 DUMMY GAUGE (Steel)
T	TEMPERATURE GAUGE

Note: 1 ft = 0.3 m. 1 in. = 2.54 cm.
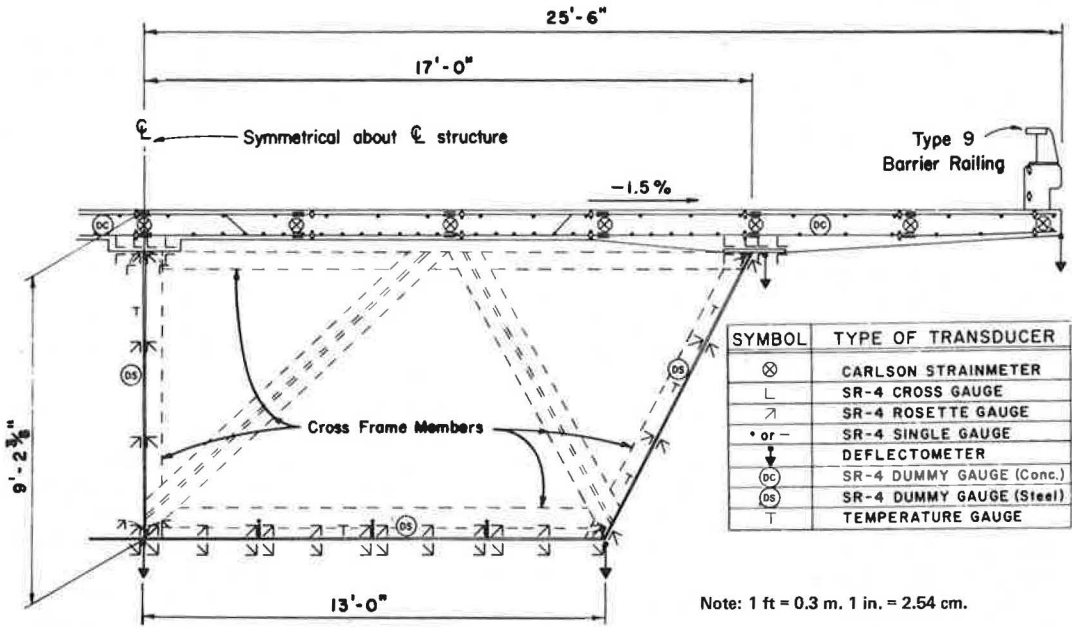
Figure 3. Profile and axle reactions for 7-axle test vehicle.

Note: 1 ft = 0.3 m. 1 in. = 2.54 cm. 1 lb = 0.45 kg.
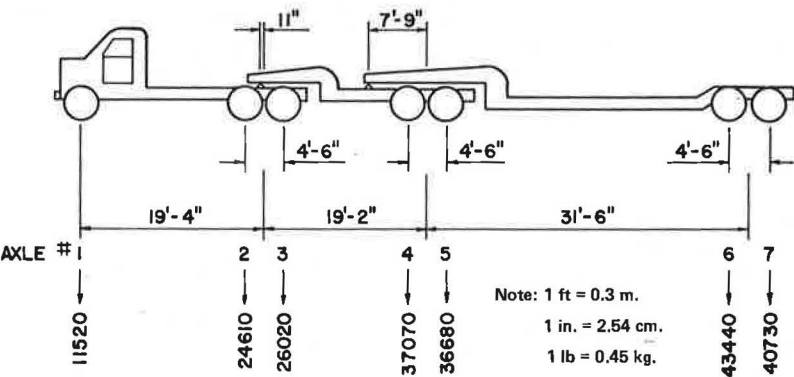
nodal points marking the intersections of webs and the mid-plane of the concrete road-
way slab. A second possible idealization existed in which flanges were moved up to the
intersections and were treated as separate plate elements with suitable modifications
in cross-sectional areas. This idealization also was applied successfully, but it will
not be discussed in this paper.

Longitudinal Live Load Strains

Membrane strains for the various concrete and steel plate elements as computed by the
FINPLA code with the 7-axle test vehicle in its leftmost transverse position on the
roadway are shown in Figure 4. Theoretical strains on opposite faces of the plates
differed very little from each other, which indicates the small influence of both general
and local bending except for relatively thick concrete roadway slab.
    Longitudinal fiber strains measured by the SR-4 gauges on the steel plate surfaces
or extrapolated from SR-4 gauges on reinforcing bars and strain meters embedded in
the concrete slab are also shown in Figure 4 for the same transverse position of the
test vehicle.
    Marked discrepancies between measured and theoretical strains were immediately
evident. Primarily, they took the form of differences in magnitudes of strains on op-
posite sides of the plates. However, plotted mean values of measured fiber strains
(mid-plane strains) exhibited marked agreement with theoretical strains.

Influence of Plate Warpage

Differences between theoretical and measured extreme fiber strains can be attributed
to the nonplanar configuration of the steel plates, which is caused by plate warpage and
dead load deflections. Such warpage is especially pronounced in webs because trans-
verse stiffeners are welded to their inner faces. The bottom plate also exhibited warp-
age between the longitudinal stiffeners. Of greater consequence was the dead load
deflection that occurred between cross frames in the bottom plate. These frames are
spaced at 22-ft (6.7-m) intervals and provide a measure of support to the plate, which
deflects between these support points under the dead load of plate and stiffeners.
    Warped plates, under the influence of tensile stresses produced by live load applica-
tion, tend to straighten and produce pronounced local bending strains, which are
superposed on the membrane strains. The bottom plate tends to assume the configura-
tion of a number of straight chords and manifests strains commensurate with upward
bending midway between these supports. The result is that tensile strains measured
on the upper surface of the bottom plate exceeded those on the lower surface, and the
tensile strains measured by the single-element SR-4 gauges atop the longitudinal
stiffeners were much greater than those on the plate even though they were appreciably
closer to the neutral axis of the box section (Figure 4). Two strain gauges mounted on
the stiffener and the plate near the cross frames exhibited the opposite behavior. The
gauge atop the stiffener produced appreciably lower strains than those on the plate,
which might be expected in the upward-curving supported plate at these points.

Transverse Live Load Strains

Theoretical and experimental transverse strains for the leftmost transverse position
of the test vehicle are compared in Figure 5. Strains in the concrete roadway slab
showed good agreement for all transverse positions except at the intersection of the
center web and the slab when no attempt was made in the theoretical treatment to
simulate slab thickening at the fillets. This decreased the measured bending strains
below those that might be expected in a slab of uniform thickness.
    Superficial comparisons of the theoretical and measured fiber strains in the steel
plates immediately suggest many anomalies. However, mean values, which represent

Figure 4. Comparison of theoretical and measured longitudinal strains for live load.

Note: 1 in. = 2.54 cm.

---- Mean Theoretical Strains
— Mean Measured Strains
△ Strains in Lower or Right Faces of Plates
+ Strains in Upper or Left Faces of Plates
✱ Strains at Tops of Longitudinal Stiffeners
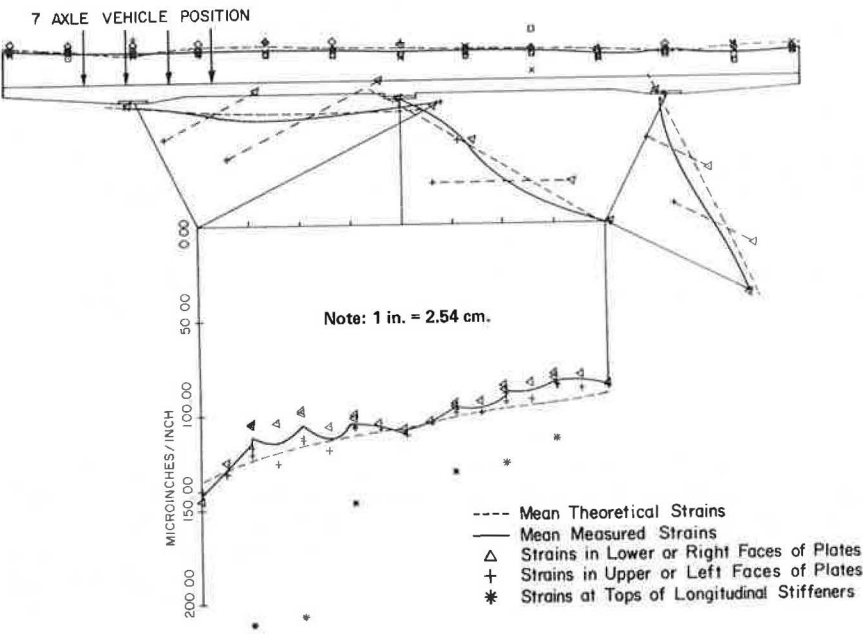
Figure 5. Comparison of theoretical and measured transverse strains for live load.

(a)

(b)

(c)

7 AXLE VEHICLE POSITION

Note: 1 in. = 2.54 cm.
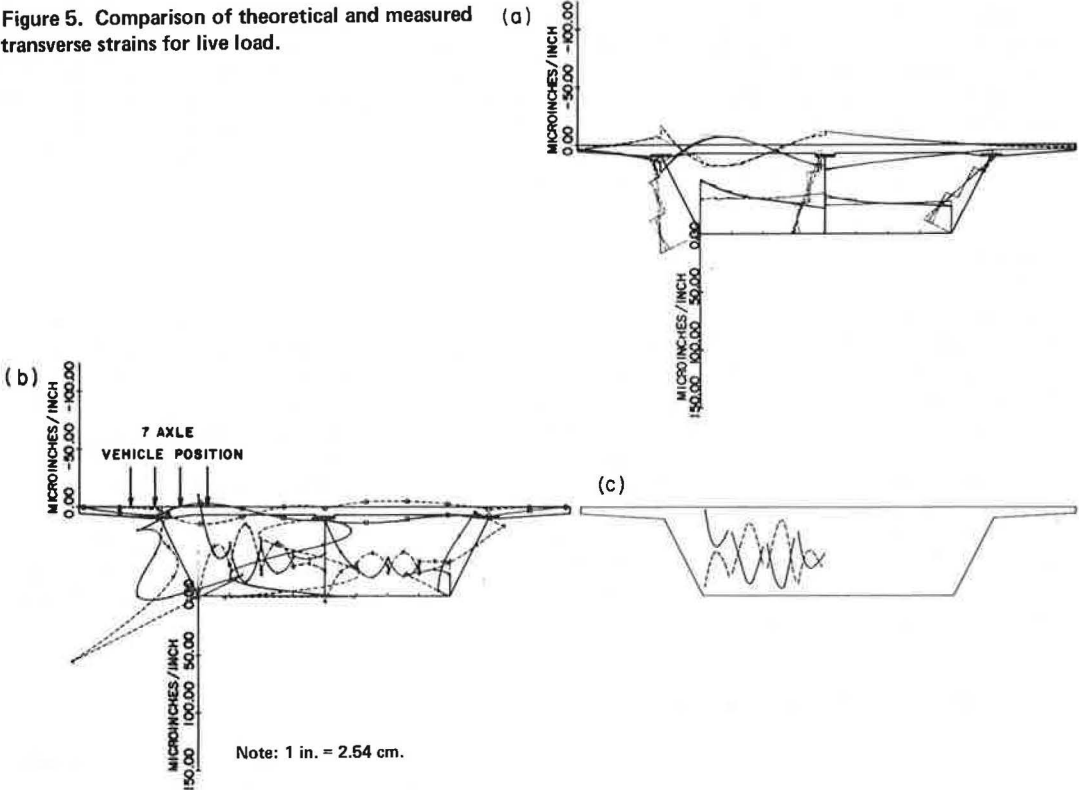
the mid-plane strains without the influence of local bending, compare favorably. Because questions have been raised frequently concerning the predictability of transverse strains in steel box girders, we tried to assess these prediction methods.

Plate warpage was assessed with some degree of precision by stretching threads at intervals along a 63-in.-long (160-cm-long) section over half the width of the bottom plate and by measuring ordinates to the plate surface. A fine finite element mesh was established by means of measured or interpolated vertical coordinates that were input at the nodes. Output displacement fields at the boundaries from the FINPLA code were then input to a structural design language (STRUDL) program. The resulting fiber strain fields are shown in Figure 5. These strains agreed with measured strains well enough in most areas to suggest that predicting transverse strain anomalies caused by plate warpage is feasible. Practically, of course, predicting maximum strains that result from statistically predicted plate warpage would be the only feasible course.

Dead Load Strains

Theoretical and measured dead load strains are compared in Figure 6. Initial comparisons indicated significant discrepancies, but a field survey revealed that the concrete roadway slab was uniformly thicker than plan dimensions by 0.1 ft (3 cm), which is about 12 percent. Figure 6 shows results of calculations revised to include the relatively significant effects of the increased load of the thicker slab on the bare steel girder. Because of the high costs of running the program, live load calculations were not repeated to assess the less significant influence of the increased stiffness caused by the thicker slab.

Theoretical strains approximated mean, mid-plane, experimental strains, but the program failed to assess anomalies caused by plate warpage and some shear lag, which occur especially in the bottom plate.

The program overestimated the torsional rigidity of the structure. Observed bottom plate strains were larger than theoretical bottom plate strains on the right, and they were smaller on the left. A similar, but much less distinct, tendency can be observed in the live load strain patterns shown in Figure 4. The aforementioned survey indicated no evidence in the slab load of imbalance toward either side of the structure. The asymmetry of the section caused by a 1.5 percent cross slope and a vertical center web were included in the programmed structure geometry.

Deflections

The same anomaly was manifested in the deflection patterns. Theoretical dead load deflections shown in Figure 7 closely approximated those measured along the right upper flange the day after the deck pour, but they exceeded those on the other 2 flanges. Dead load deflections increased because of creep and shrinkage of the slab. Deflections measured 6.5 months after the pour agreed more closely with theoretical deflections at the center web. Measured deflections were greater than theoretical deflections on the right and smaller than theoretical deflections on the left. This anomaly also resulted in curves of theoretical live load deflections as functions of transverse test vehicle position that were significantly flatter than those for measured deflections (Figure 8). The excessive stiffness of the section caused by the thick deck slab, which, as noted previously, was not included in the program, produced theoretical deflections that were uniformly greater than those observed.

SUMMARY AND CONCLUSIONS

With minor exceptions, differences between measured and theoretical deflections and strains were within customary design tolerances. Accurate assessment of fiber stresses requires predicting plate warpage. One project objective entailed determining

Figure 6. Comparison of theoretical and measured longitudinal strains for dead load of roadway slab on bare, steel box section.

.... Theoretical Strains on Bottoms or Right Faces of Plates

—··—·· Theoretical Strains on Tops or Left Faces of Plates

△— — — Experimental Strains on Bottoms or Right Faces of Plates

+——— Experimental Strains on Tops or Left Faces of Plates

✳ Strains at Tops of Longitudinal Stiffeners

Note: 1 in. = 2.54 cm.
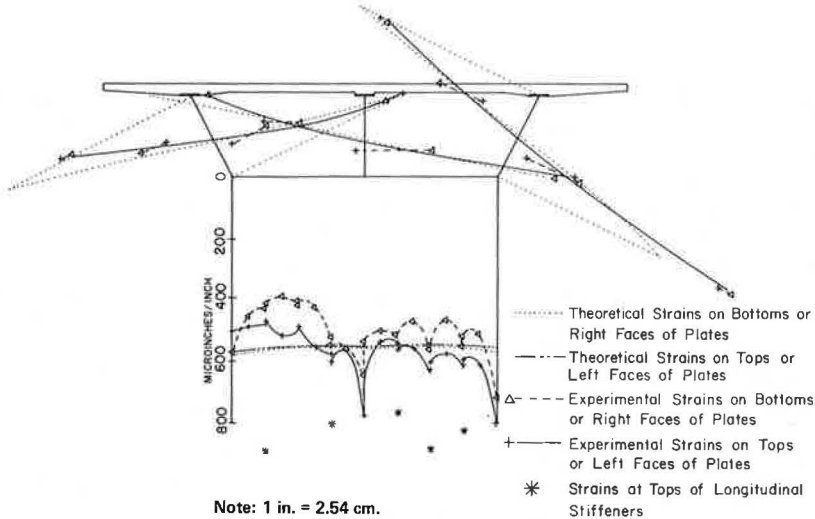
Figure 7. Theoretical and measured dead load deflections.

— — — 1 Day
—·—·— 6½ Months
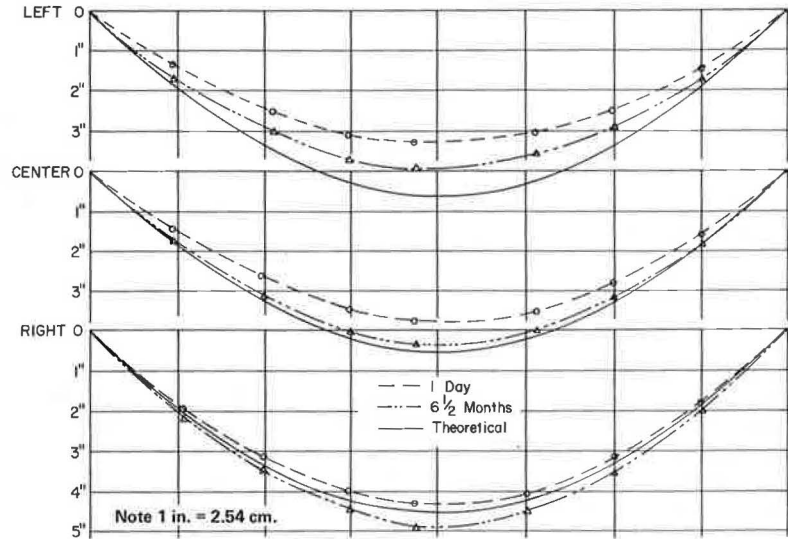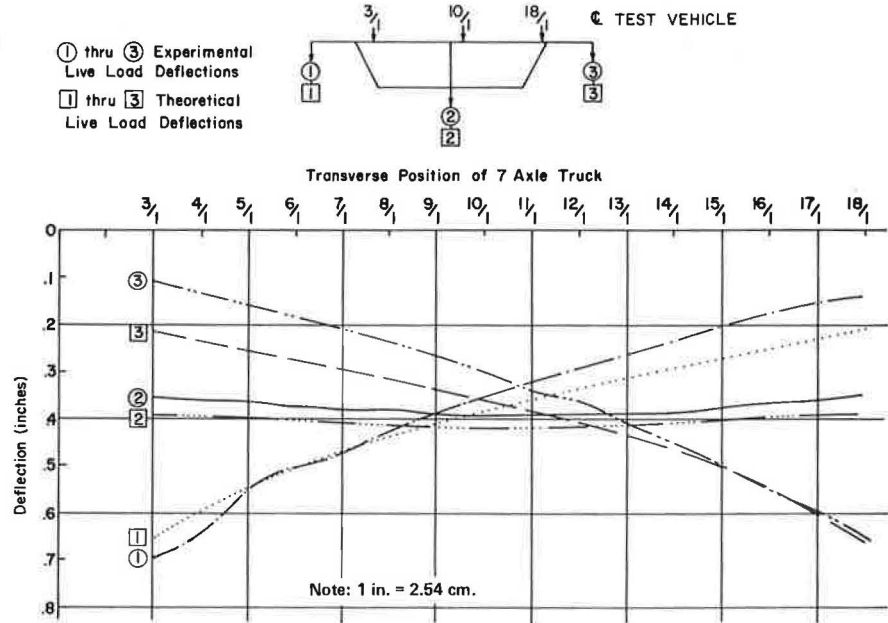——— Theoretical

Note 1 in. = 2.54 cm.

Figure 8. Theoretical and measured live load deflections at 3 nodes as functions of transverse position of test vehicle.

① thru ③ Experimental Live Load Deflections

☐1 thru ☐3 Theoretical Live Load Deflections

₵ TEST VEHICLE

Transverse Position of 7 Axle Truck

Note: 1 in. = 2.54 cm.

distribution factors for this type of structure. However, previous studies have demonstrated that the distribution factors that employ only stringer spacing may ignore other factors that have important influence in characterizing live load distribution (4). Moreover, in a structure having sloping webs, as most steel box sections do, some question might arise concerning the dimensions for stringer spacing.

The gross moment of inertia method used in the original design of the tested prototype offers little provision for accurate assessment of the true distribution characteristics of the cellular box section and is, as a consequence, somewhat conservative. Moreover, the method cannot provide even approximate values of transverse stresses. We believe that future designs of this type of structure could be improved and that significant economies could be realized in design by applying proven numerical procedures comparable to the procedure described in this paper.

Because few composite steel box girders are designed in the United States and because of the reasonable agreement between theoretical and measured strains in this study, we recommend that those engaged in design and analysis of such structures use sophisticated, computerized, finite element codes such as FINPLA instead of distribution factors that may have questionable theoretical bases.

ACKNOWLEDGMENTS

REFERENCES

1. R. E. Davis and G. A. Castleton. Load Distribution in a Composite Steel Box Girder Bridge. California Division of Highways, Rept. CA-HY-BD-4137-73-7, June 1973.
2. A. C. Scordelis. Analysis of Continuous Box Girder Bridges. Univ. of California, Berkeley, Rept. SESM 67-25, Nov. 1967.
3. C. Meyer and A. C. Scordelis. Computer Program for Prismatic Folded Plates with Plate and Beam Elements. Univ. of California, Berkeley, Rept. SESM 70-3, Feb. 1970.
4. A. C. Scordelis, R. E. Davis, and K. S. Lo. Load Distribution in Concrete Box-Girder Bridges. In Concrete Bridge Design, American Concrete Institute, Publication SP-23, 1967.

LABORATORY EVALUATION OF FULL-SIZE, ELASTOMERIC, BRIDGE BEARING PADS

W. F. Crozier, J. R. Stoker, V. C. Martin, and E. F. Nordlin,
Division of Construction and Research, California Department of Transportation

Elastomeric, bridge bearing pads, which were reinforced by layers of steel, fiberglass, or polyester cloth, were evaluated by laboratory testing. Full-size specimens were loaded in simulated service conditions. Steel and fiberglass reinforcement showed decided superiority.

ABRIDGMENT

•ELASTOMERIC pads were first used as bridge bearings in the United States in the late 1950s generally because a satisfactory bearing device that could accommodate the relatively severe end rotation and translation associated with prestressed concrete structures was needed. Bearings more economical and maintenance free than those used previously also were desired. At that time, California started a research project to establish design guidelines and specifications for these pads (1). That study revealed that neoprene pads reinforced at $\frac{1}{2}$-in. (12.7-mm) intervals with steel sheet or polyester fabric performed satisfactorily in the bridges constructed during that period. The polyester fabric became the most commonly used reinforcement in California. Polyester fabric is less expensive than steel because large pads can be fabricated, stockpiled, and sliced into custom sizes on demand. Steel-reinforced pads must be fabricated individually to the desired size because the edges of the steel must be covered with elastomer for corrosion protection.

During the 1960s, use of prestressed concrete bridges became more common and typical span lengths became longer because of designers' interest in economy, safety, and aesthetics. Consequently, bearing pads became larger in both plan area and thickness to accommodate increased loads, translations, and rotations. As pad sizes increased, construction personnel began to notice pad deflections that were considerably different from those anticipated. At that time pad deflections were predicted on the basis of tests performed on relatively small pads. Some design data (2) were extrapolated to estimate the behavior of the pads being used. When it became apparent that extrapolation of data from small pads would not ensure satisfactory performance of large pads, the research project that will be discussed in this paper was initiated to evaluate the physical characteristics of full-size bearing pads and to modify the pertinent specifications and design criteria if necessary.

The objective of this research was to evaluate the performance of full-size bearing pads under test conditions simulating actual field use. Various shapes and sizes of pads up to 7 ft^2 (0.65 m^2) in plan area and 5 in. (127 mm) in thickness were subjected to compressive, cycling, creep, translation, rotation, and ultimate-strength tests. Typical pads consisted of 55-durometer-hardness neoprene reinforced at $\frac{1}{2}$-in. (12.7-mm) intervals with steel, polyester, or fiberglass reinforcement.

This abridgment is a condensed version of a more detailed paper that is available elsewhere (3).

CONCLUSIONS

These conclusions are based on laboratory testing at approximately 70 F (21 C) and apply to pads fabricated in accordance with California specifications (3). The pads exhibited 55 ± 5 durometer hardness (ASTM D 1149, type A); they were reinforced at intervals of $\frac{1}{2} \pm \frac{1}{8}$ in. (12.7 ± 3.2 mm). Reinforcement was fabric or 20-gauge (0.91-mm) mild steel with a minimum ultimate tensile strength of 700 lb/in. (122.5 kN/m) at top and bottom of pad and 1,400 lb/in. (245 kN/m) within the pad.

Polyester-Reinforced Pads

Compressive deflection of polyester-reinforced pads is difficult to predict accurately for 4 reasons.

1. Magnitude of deflections of polyester-reinforced pads is much greater than that of steel- or fiberglass-reinforced pads because of the relative tensile flexibility of the polyester fabric.
2. Compressive stiffness decreases as overall pad thickness increases.
3. Compressive creep of polyester-reinforced pads under sustained dead load stresses is 2 to 3 times that of steel- or fiberglass-reinforced pads because of polyester fabric creep.
4. Compressive deflections due to live load cycling tend to remain in the pad after the live load is removed.

Translation and ultimate strength properties of polyester-reinforced pads are similar to those of fiberglass-reinforced pads.

Fiberglass- and Steel-Reinforced Pads

The following conclusions hold for fiberglass- or steel-reinforced pads:

1. Compressive deflections can be reliably predicted within the normal range of construction tolerances;
2. Compressive stiffness is not significantly dependent on overall pad thickness;
3. Compressive creep under sustained dead load stresses is approximately 25 percent of initial deflection after 10 years of service;
4. Compressive deflections due to live load cycling tend to diminish after live load is removed;
5. Ultimate compressive strength is more than 1,600 lb/in.^{2} (11 040 kPa) (mode of failure is fabric tearing or steel yielding);
6. Under a nominal compressive load of 800 lb/in.^{2} (5516 kPa), fiberglass- or steel-reinforced pads may be subjected to rotational forces until compressive strain at an extreme edge is 0 without damaging the pad; and
7. Shear modulus is approximately 100 lb/in.^{2} (690 kPa) at 70 F (21 C). This value is not significantly dependent on pad size, shape, skew angle, or compressive stress.

RECOMMENDATIONS

Polyester-reinforced pads more than 1 in. (25 mm) in thickness should not be used in bridge bearings because they make it difficult to predict compressive deflection.

For pad thicknesses normally used in bridge construction, steel- or fiberglass-reinforced pads should be specified in accordance with the specifications presented elsewhere (3).

Compressive deflections for steel- or fiberglass-reinforced pads should be predicted by using the data shown in Figure 1. The accuracy of these curves is considered to be

Figure 1. Recommended compressive stress-strain curves for
steel- or fiberglass-reinforced pad of 55 durometer neoprene.
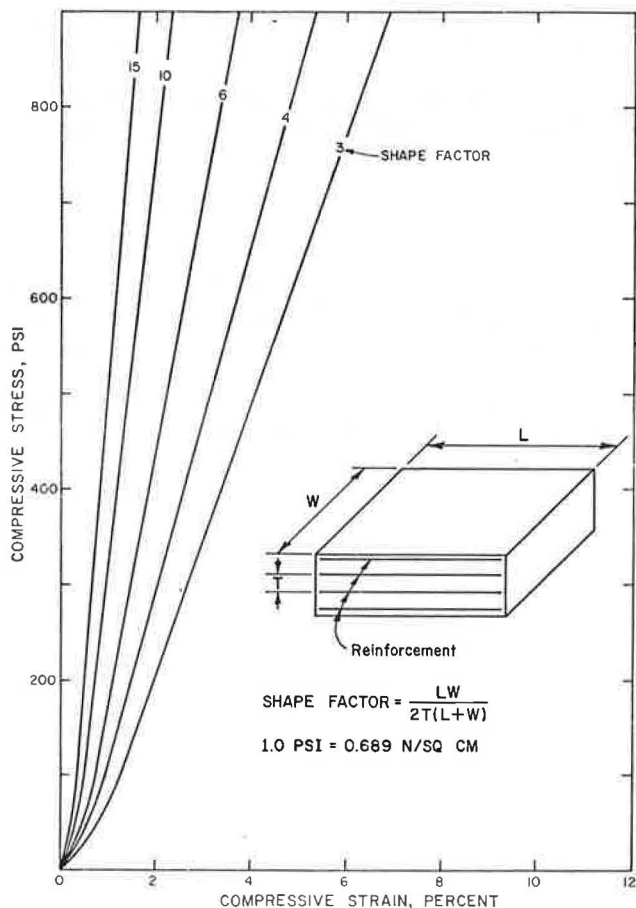
well within the range of normal construction tolerances. If long-term compressive
creep is to be included in the prediction, then the values obtained from Figure 1 should
be increased by 25 percent. For special situations requiring extreme accuracy, sample
pads should be tested to determine the stress-strain behavior of each lot of pads.

Further research is needed to improve specifications and test methods used to
ensure the quality of bridge-bearing pads. Based on field performance to date, current
specifications and test methods result in high-quality pads, but these requirements
vary considerably throughout the nation. Some tests are difficult or expensive to
perform, and, in some cases, requirements may be unnecessarily conservative and
restrictive. Research is needed to develop simple and inexpensive test methods of
performance requirements.

If further research is contemplated for large bearing pads, careful consideration
must be given to test method details (3).

The recommendations on pad thickness were implemented by the California Depart-
ment of Transportation in late 1972. Since that time, there have been no reports of
adverse performance of fiberglass-reinforced pads.

58

ACKNOWLEDGMENTS

REFERENCES

1. E. F. Nordlin, J. R. Stoker, and R. R. Trimble. Laboratory and Field Performance of Elastomeric Bridge Bearing Pads. California Division of Highways, Jan. 1968.
2. Design of Neoprene Bridge Bearing Pads. E. I. du Pont de Nemours and Co., Inc., April 1959.
3. W. F. Crozier, J. R. Stoker, V. C. Martin, and E. F. Nordlin. A Laboratory Evaluation of Full Size Elastomeric Bridge Bearing Pads. California Department of Transportation, 1974.

IRIS—AN INFORMATION RETRIEVAL SYSTEM FOR BRIDGE INVENTORY MAINTENANCE

Charles J. Conley, Colorado Department of Highways;
Jerome C. Kaltenhauser, University of Colorado; and
E. W. Klaphake, Sperry-Univac

The Colorado Department of Highways bridge structure inventory has been automated by using the IRIS information storage and retrieval program. IRIS allows rapid and convenient bridge inventory updates and maintenance, selective retrieval of information for report generation, and on-line queries of the data bank. IRIS maintains its principal data bank as a pseudo-inverted list structure on mass-storage devices. Selection of records for retrieval is made by calculation rather than by file search and comparison, and the selected records are reconstructed rather than retrieved as entities. Each category of information (descriptor) is a candidate for use as a key for retrieval, so maximum flexibility and specificity are possible in describing records for retrieval. The user describes a set of bridge records for retrieval by involving 1, some, or all of the descriptors as retrieval keys in Boolean expressions by using a simple and convenient language. Records that belong to the described set are retrieved. The generality of the IRIS design allows it to be used in many applications other than bridge inventory. IRIS is written in FORTRAN and is operational in both batch and interactive modes on the CDC 6400 at the University of Colorado.

•EACH state highway department is required by Section 26 of the Federal-Aid Highway Act of 1968 to develop an inventory of all bridges in the state carrying or spanning a federal-aid highway. At intervals of a year or less, several different reports on the inventoried bridges must be submitted to the Federal Highway Administration. Bridge inventory maintenance and report-generation requirements are being met by the Colorado Department of Highways by the computer program IRIS and associated report-generation programs.

IRIS maintains the state bridge inventory for fast access in a data bank on mass-storage devices (disks) rather than magnetic tapes. Correction facilities are provided to allow the inventory to be rapidly updated as errors are found and new information on bridges is acquired. Retrieval of bridge data is by way of a simple Boolean language that enables the user to specify the kind of bridges he or she wants retrieved in terms of the information stored about each bridge. The user can request that the retrieved bridges simply be counted, that some or all of the information on each retrieved bridge be printed out, or that some or all of the information be placed in a machine-readable file for processing by auxiliary programs such as report generators.

IRIS can operate in an interactive mode as well as a batch mode. The interactive mode enables the user to explore the bridge inventory through successive queries, and answers return in a matter of seconds. A dialogue with the inventory in which the user asks the questions is allowed by the simplicity of the query language and the rapid response to queries in the interactive mode.

IRIS was acquired and developed by the Colorado Department of Highways for bridge inventory and reporting requirements, but it has potential for being implemented by a much wider range of users. The data structure and format are quite general—the parent program, TAXIR, from which IRIS descended, was developed for handling taxonomic information in botany (1)—and program capabilities can be extended in several directions with minor modifications.

This paper addresses 2 audiences: bridge engineers responsible for maintaining bridge information and data processing personnel responsible for facilitating the maintenance of the information.

BRIDGE INVENTORY APPLICATIONS

Data Description

The Colorado Department of Highways bridge inventory is coded in accordance with the Recording and Coding Guide for the Structure Inventory and Appraisal of the Nation's Bridges (2). Each structure in the inventory is represented by a record of 84 items or descriptors that convey various types of information. The following example descriptors are taken from the Recording and Coding Guide (2):

1. Identification, which includes information on inventory route, structure number or designation, features intersected by the structure, local topography (narrative description), and latitude and longitude of the structure;
2. Structural data, which include information on year built, design load, and average daily and yearly traffic;
3. Type of structure, which includes information on materials, bridge structural type, and number of spans;
4. Condition, which includes information on operation rating, condition of deck, and condition of superstructure; and
5. Proposed improvements, which include information on estimate of year needed, proposed design of improvements, and estimated cost of improvement.

The information carried by the items in the Recording and Coding Guide (2) is in the form of either character strings or integers, but 3 kinds of descriptors will be distinguished to clarify some characteristics of the IRIS program. A character string can be either a name or text, but in IRIS usage a name is a character string that the user expects to occur in more than 1 record. For instance, because there are many bridge structures in Denver, Colorado Springs, Pueblo, and other cities, the names of these cities would recur in many bridge records. Text is also a character string, but no such recurrence is expected. Certain items in the data bank call for descriptions of features near a bridge, and, because the user is free to improvise, any recurrence of a character string would be by chance. This is an example in which a character string would be regarded as text. IRIS allows name character strings of up to 90 characters and text character strings of up to 40 characters for any item. (These limits can be varied at will by simple program changes.) Integer numbers have the usual properties of integers and can express virtually any magnitude. The restriction to integer values of numbers is not serious because a simple program modification would allow decimal input. Decimal output is currently an option of the program.

Query Description

Until now the terms item and descriptor have been used interchangeably to designate a category of information; the term item is from the Recording and Coding Guide (2). In this paper, it will be convenient to use the term descriptor exclusively. The information carried by a descriptor is designated a descriptor state and can be thought of as

an entry under the descriptor. Each descriptor has a descriptor state or entry in each bridge structure record in the bridge inventory data bank. For example, for the descriptor, average daily traffic, 1,231 might be the descriptor state in a particular bridge record. Figure 1 shows the relation of descriptors, descriptor states (S_{1j}'s), and bridge records. This figure shows a bridge inventory in abstract form as a large table that has all the information on a single bridge written on a single line.

Queries on bridge inventory require that the user specify the kind of bridge in which he or she is interested. Bridge records meeting the specification are identified for further processing. IRIS query specifications are written by involving 1 or more descriptor states in a Boolean expression by using the Boolean operators, OR, AND, and NOT. The simplest possible Boolean expression is the name of the state in which the user is interested. Because the program must be informed of the descriptor to which the state belongs, the descriptor also must be named. This forms a descriptor-descriptor state pair. A query containing the information average daily traffic, 1,231 would identify all bridges with an average daily traffic of 1,231 vehicles. If the user is more interested in a range of traffic conditions, he or she might write average daily traffic, from 1,000 to 1,500, and all structures that have average daily traffic from 1,000 to 1,500 vehicles would be identified.

Query specifications of greater complexity can easily be written by using the Boolean operators in the conventional way. The user might be concerned with heavily used bridges. He or she would write a Boolean expression that would be set up as follows: (average daily traffic, from 2,000 to 5,000) AND [(number of lanes, 1) OR (number of lanes, 2)]. Bridges with 1 or 2 lanes carrying 2,000 to 5,000 vehicles per day would be identified. If the user is interested in only a particular highway or section of a highway, the highway and section numbers would be incorporated into the expression by using AND operators. The expression can incorporate as many terms as the user needs to single out the bridge or bridges in which he or she is interested. There is no restriction on which descriptors and states are entered into the retrieval expressions.

Retrieved queries return either a count of the records that meet the user's specification or part or all of each such record. A sequence of queries to determine whether any structures on US-6 have a rating of 30 tons (27 metric tons) or less for 3-axle rigs was performed. Because some of the structures do have such a rating, additional information identifying the particular bridges, their structural conditions, and length of detour necessary was requested. Some terms used in the actual queries have been changed for clarity but the essentials remain. In the sequence of queries shown in Figure 2, a set of records (bridges in this case) is selected at each stage, and each successive set is a subset of the set from the previous query. In IRIS the word RESULT is reserved to designate the set of records from the previous query. Therefore, when RESULT appears in the Boolean expression, it means that subsequent queries will be made only on the set of records identified in the previous query. Figure 2 shows this series of queries. The limiting structures and length of detours are now identified. Subsequent queries on the detour routes would reveal whether they will accept the vehicle of interest. In the illustrated queries the user added some comments to the query language to aid later interpretation.

The principal use of IRIS by the Colorado Department of Highways is for storing and reporting on the required state bridge structure inventory, and for this purpose the retrieved records are placed in a machine-readable file for processing by auxiliary report-generating programs. The user controls which records will be retrieved by the Boolean specification he or she writes, and the user controls which portion of each record is to be retrieved by a descriptor list. In query 3 in Figure 2, for example, the user requested that information on only 4 descriptors (out of 84 in the data bank) be reported. In retrieving information with IRIS the user has control over which bridge structure records, each of which contains information on 1 bridge, are to be retrieved and which information is to be reported for each record.

Figure 1. IRIS data format.

Figure 2. Series of queries.

1. HØW MANY STRUCTURES HAVE (HIGHWAY, US 6)*

    NØ. ØF RECØRDS IN QUERY RESPØNSE = 92

    NØ. ØF RECØRDS IN THE DATA BANK = 3719

2. HØW MANY STRUCTURES WITH (AXLE, 3) AND (WEIGHT, FRØM 00 TØ 30)

    AND RESULT*

    NØ. ØF RECØRDS IN QUERY RESPØNSE = 2

    NØ. ØF RECORDS IN THE DATA BANK = 3719

3. PRINT A LIST ØF INFØRMATIØN ABØUT ABØVE: (FEATURES INTERSECTED

    STRUCTURE NUMBER, DETØUR LENGTH, STRUCTURAL CØNDITIØN) AND RESULT*

    MCDØNALD CREEK H-01-U   99   4

    BIG SALT WASH   H-02-V   6   6

IRIS PROGRAM DESCRIPTION

Figure 1 shows the general data format assumed by IRIS. The descriptors are categories of information such as structure number or number of lanes. A record is built up from the entries under each descriptor and is therefore the description of a particular bridge structure or other object of interest handled by the program. IRIS must transform, store, update, and retrieve records under user control. Retrieved records also must be presented to the user in a useful form.

Each entry S_{ij} in Figure 1 is called a descriptor state. A descriptor state can be an integer or a character string in IRIS. A consequence of the IRIS data format is that a particular descriptor can have 1 and only 1 state in a given record. The format also makes possible a compact method of data storage and a fast and flexible retrieval mechanism.

The storage mechanism in IRIS depends on the idea of mapping 1 finite set of elements into another. If a given descriptor has a finite number of states, then all possible states for that descriptor can be set in a 1-to-1 correspondence with the positive integers. There are various ways of making the correspondence, but, if the correspondence rule is chosen to have an inverse, then the passage from any descriptor state to its sister element among the positive integers can be made and the inverse passage from the domain of positive integers to descriptor states also can be made.

When all the name states of a descriptor are arranged in alphabetical order in a dictionary, the dictionary entries can be mapped into the positive integers in a natural way by assigning 1 to the first entry, 2 to the second, and so forth. Conversely, if 1 of the positive integers i within the range of the dictionary is given, then the descriptor state can be found immediately. It is the i th dictionary entry. Because equally spaced integers or decimal numbers representing measurements (or any ordinal numbers, generally) are inherently ordered, mapping into the positive integers 1, 2, 3, ... can be carried out quite naturally. Text differs from ordered numbers (orders) and names in that the size of the set of different states that might be encountered is not known beforehand. This is, in fact, the essential distinction between text and name descriptors in the IRIS program.

When the mappings for order and name descriptor states are completed, the integer corresponding to any state of a descriptor having N different states can be expressed in $W = \lfloor \log_2 N + 1 \rfloor$ bits (the brackets denote truncation to the nearest lower integer unless $N = 1$). In other words, the N different states that a descriptor can assume are enumerated 1, 2, 3, ..., N, and this requires $W = \lfloor \log_2 N + 1 \rfloor$ bits. IRIS uses the integers discussed here to store the order and name states in each record and to retrieve, or, rather, to identify and reconstruct, records having user-specified characteristics. If the records in a data bank use m descriptors, then m integers in binary form are stored for each record; a descriptor with N_n possible states is allotted $W_n = \lfloor \log_2 N_n + 1 \rfloor$ bits for a binary integer. The stored binary integers are designated chi string functions (CSFs). One CSF per descriptor is stored for each record.

To reconstruct the actual descriptor states, as is done in retrieval, the mapping process is reversed. For an order descriptor, a linear transformation of its CSF gives the state represented. For a name descriptor, the CSF is the index of the literal state name in the dictionary maintained for the descriptor. Text descriptor states cannot be mapped into the positive integers in the same fashion as orders and names can, so they are stored full length in character representation. This uses space rapidly, so for extensive amounts of text a document file would have to be coordinated with the primary data bank.

In what is commonly called an inverted list data structure, information used in retrieval is kept separate from the stored records so that identification of records for retrieval can be made without inspecting the records themselves. In IRIS the situation is similar, except that the records are not stored as entities—they are decomposed into CSFs plus dictionaries. This has been called a pseudo-inverted list-information structure. Because each descriptor used in the data bank is on the same basis as every other, each descriptor is suitable as a candidate for use as a retrieval key. Also only those descriptor states of interest to the user need to be reconstructed in the interval records.

Because the identification of records for retrieval is a somewhat involved process to describe, we will present only a brief sketch. The user supplies to the program a Boolean expression that describes a set of records in terms of the descriptor-descriptor state combinations of his or her choosing, and the program must determine which records, if any, are members of the described set. The user-supplied Boolean expression is transformed by IRIS into a Boolean function for operation on the successive CSFs corresponding to the descriptors involved. The Boolean function allows the examination of the CSFs using OR, AND, and NOT machine operations. Any record identified by these operations is flagged for selective reconstruction.

A brief look at the actual disposition of the data bank in storage should further clarify IRIS retrieval operations. The dictionaries are presently kept in core. The CSFs are kept in mass storage and are brought into core as needed for retrieval and other operations. The buffer used for mass storage transfers is shown in Figure 3 for CDC 6000 series machines. Each row in Figure 3 corresponds to 1 computer word, and the 60 bits of a word correspond to the 60 columns shown in the figure. Each of the columns contains one data bank record. That is, all the CSFs for a given record are stored vertically in a column: The first W_1 bits down are for the CSF of descriptor 1, the next W_2 bits down are for descriptor 2, and so on. The current Colorado Department of Highways data bank requires a buffer of approximately 1,400 words for its 84 descriptors.

The identification of records for retrieval or reconstruction was described previously as though 1 record were processed at a time. In actuality, because of the full word orientation of the OR, AND, and NOT machine operations involved, all columns in a buffer are processed simultaneously. Thus, 1 sweep through the buffer determines which of the 60 records should be reconstructed.

Figure 3. IRIS data bank buffer.
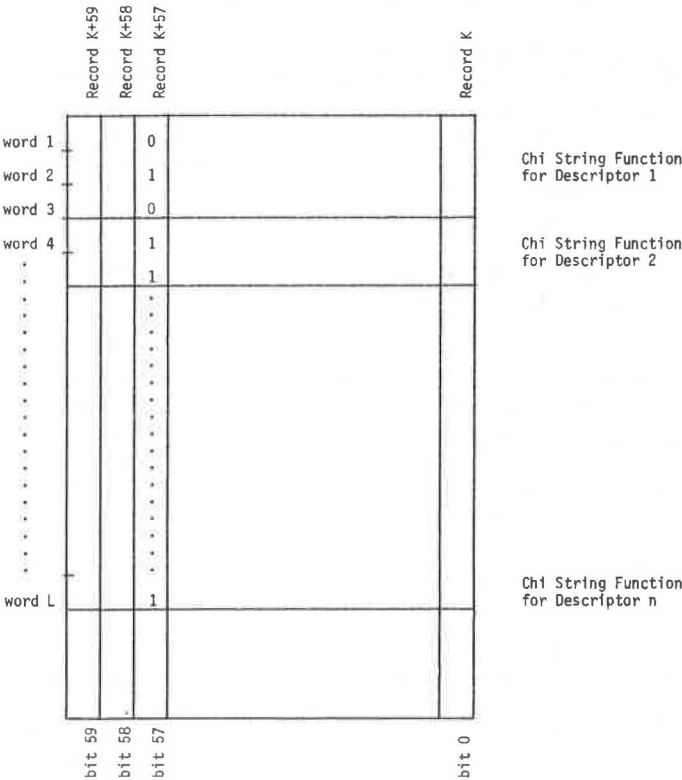
IMPLEMENTATION

IRIS is written in FORTRAN and has 1 mass-storage random-access routine in assembly language. The primary data bank is placed in mass storage. In the batch mode, data bank corrections are transformed, accumulated, and placed in extended core storage (ECS) to allow all corrections to be made in 1 sweep through the data bank. ECS is not used when one is making corrections in the interactive mode, so each correction requires a pass through the data bank. Except for this, batch and interactive modes are completely equivalent. For the bridge inventory application, only 100 words (each word has 10 characters) are allotted to the name descriptor dictionaries. Allowing for up to 120 descriptors, this version of IRIS requires 46,000 (octal) 60-bit words of core storage to run. The program also uses up to 32,000 (octal) words of ECS when making corrections in the batch mode. The length of the buffer used to transfer information from mass storage to core is set not by the word size of the machine but by the number of states the user allows for various descriptors (roughly following the $\log_2$ dependence previously described). It was noted that a 1,400-word buffer handles 60 bridges (60 bits per word in CDC 6000 series machines). There are 3,700 bridges in the inventory. Therefore, sixty-two 1,400-word buffer loads ($60 \times 62 > 3,700$) must be transferred from disk file to core. This set of transfers is required whether the operation is a simple query, a complex query, or the dumping of the entire data bank to a report file.

IRIS capacity is virtually unlimited in 2 directions: the number of order descriptor states (because for ordered numbers the $\log_2$ dependence describes total growth in storage required) and the number of records that the program can maintain. Core storage increases would be in direct proportion to space additions for large name dictionaries.

Some simple cost figures, although they are heavily dependent on the particular equipment and charging algorithms used, may help to convey an idea of user charges. For simple queries, like those illustrated in this paper, central processor times are about 0.2 s per query and cost 2 cents apiece. The corresponding mass-storage charge for a single query on the data bank (as opposed to the RESULT of a previous query) is about $1.00. The high mass-storage charge reflects a charging algorithm with high overhead for accesses and low charges for information transfer. As noted above, the mass-storage charges are incurred only in moving the data bank and are unrelated to the complexity of the retrieval operations carried out. Greater complexity in these operations is reflected in increased central processor costs. To dump the entire data bank to a formatted report file and to the printer costs approximately $80.00, a large part of which represents central processor and printer costs.

REFERENCES

1. G. F. Estabrook and R. C. Brill. The Theory of the TAXIR Accessioner. Mathematical Biosciences, Vol. 5, 1969, pp. 327-340.
2. Recording and Coding Guide for the Structure Inventory and Appraisal of the Nation's Bridges. National Bridge Inspection Standards, Article 25.11, Federal Register, Vol. 36, No. 81, p. 7851, April 27, 1971.

BRIDGE PIER STAINING

Sam I. Thornton, Department of Civil Engineering,
University of Arkansas

The Arkansas Highway Department studied bridge pier staining to deter-
mine the cause of stains, their effects on structures, and the best methods
of preventing and cleaning stains. A letter survey of other states and
tests on Arkansas bridges were included in the study. Runoff from the
bridge deck is the primary cause of bridge pier stains. Arkansas stains
contain the elements normally found in soil, rust, and tires. No significant
structural damage was found in Arkansas, but some damage, primarily
from salt, was reported in the other states. Methods suggested to prevent
runoff water from bridge piers include use of continuous spans, expansion
joints placed away from piers, preformed seals, and abutment drains.
Three-fourths of all bridge stains can be removed by washing. Rust stains
and graffiti, however, can be removed only by costly chemical procedures
or sandblasting.

•A STAINED or discolored bridge can look old before its time and will give the ap-
pearance of being dirty or unkept. Stains also may indicate deterioration of the bridge
structure. In an effort to find solutions to the problem of bridge pier staining, the
Arkansas Highway Department funded a study to determine the following (1):

1. Cause of bridge pier stains,
2. Effects of stains on structures,
3. Methods of preventing stains, and
4. Methods of cleaning stains.

SURVEY OF STATES

A letter survey on bridge stains was sent to the 49 states other than Arkansas, and
the District of Columbia. The survey asked for the states' experiences on composition,
origin, effects, and prevention of bridge pier stains. Forty of the states replied, and 5
of the replies reported that they had no information to offer.

Most reports stated that most stains were composed of iron and salt. Rust was the
most common stain, but weathering of iron pyrite in aggregate also was reported. Salt
from roadway deicing was the second most common cause of stain.

Stains also were reported from fungus, bird droppings, waterborne minerals,
petroleum products, dust, clay, marine growth, calcium carbonate, concrete or grout
salts, and joint sealants.

Leakage of expansion joints was reported to be the most common source of stain.
Weathering of concrete and paint breakdown also were reported as being common.

Fifteen of the respondents reported only aesthetic damage; 8 reported serious de-
terioration in some cases. Four of the 8 reporting damage listed salt or salt wastes
as the cause. From the remaining 4, 1 blamed scaling and spalling, 1 blamed drainage,
1 blamed weathering, and 1 did not list a cause. The remaining respondents considered
structural damage as a minor problem only.

Most suggestions to prevent stain or discoloration are to eliminate water through the joints. Designing more effective drainage systems, sealing all joints, and eliminating joints by use of continuous-span bridges were suggested. Other preventive measures include using waterproof membranes to seal concrete and galvanizing exposed anchor bolts and bearing plates. Where weathering is involved, limiting the amount of iron pyrites and shale in aggregates is suggested.

Only 2 systems of treating bridges that already were stained were suggested. One respondent suggested removing stains with muratic acid and then treating them with a 50 percent-50 percent solution of boiled linseed oil and mineral spirits. The other suggested either sandblasting and treating the caps with epoxy paint or biannually washing areas and then treating them with a solution of linseed oil and mineral spirits.

ARKANSAS STUDY

Stain Composition

Three general types of concrete stains were found in Arkansas: rust stain, graffiti, and broad red or gray stains. These stain types account for more than 99 percent of all discoloration on bridge piers, aprons, and supporting members.

Composition of the stains was determined by qualitative chemical tests, combustion, and x-ray analysis. Rust stains (those directly traceable to metal rust) contained iron compounds and were the familiar burned red or rust color. The broad red and gray stains contained compounds of iron, sulfur, potassium, aluminum, silica, and calcium (Figure 1).

Stain Origin

Rust stains resulted from rusting steel in the bridge structure. Rust stains occurred at the anchor bolts, bridge expansion joints, and bridge piers and on the apron at the end of bridges. Several examples of rust stains that occurred before the bridge deck was placed were found on concrete aprons. Almost all of the rust stains on bridges were below places on the bridge that are difficult or impossible to paint.

Red and gray stains were the result of weathering and surface runoff. The stains occurred in areas where runoff from bridges wet concrete surfaces. In addition, the composition of the stains (iron, silica, aluminum, and sulfur) indicated that soil and road grime were the origin. The presence of sulfur is not surprising because it is used in the manufacture of tires (1 to 1.5 percent by weight) and occurs naturally in asphalts (usually less than 1 percent by weight). Inspection trips during and just after showers confirmed that areas of red and gray stains were wet by surface runoff.

Extent of Stains

No significant structural damage as a result of stains was found on the Interstate bridges during the inspection trips. Stains were superficial and did not penetrate the concrete or accompany a deterioration of aggregate. A small amount of deterioration was present, however, above the rust stains. Rocker arms, anchor bolts, and bearing plates were the most frequent cause of rust stains.

Cleaning

Graffiti and rust stains were difficult to remove. Sandblasting is an effective method of stain removal, but it removes part of the concrete. When repeated often, sandblasting removes the concrete matrix. Derrington, Stowe, and Miller (2) recommend using

68

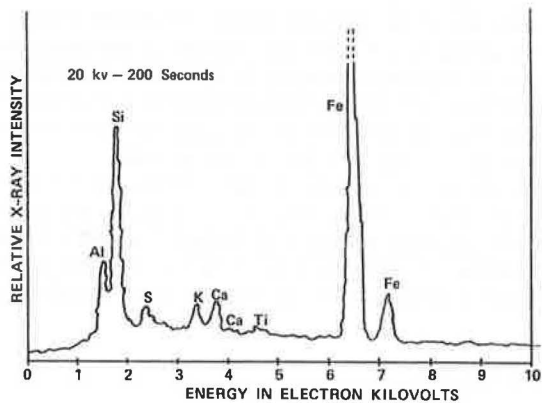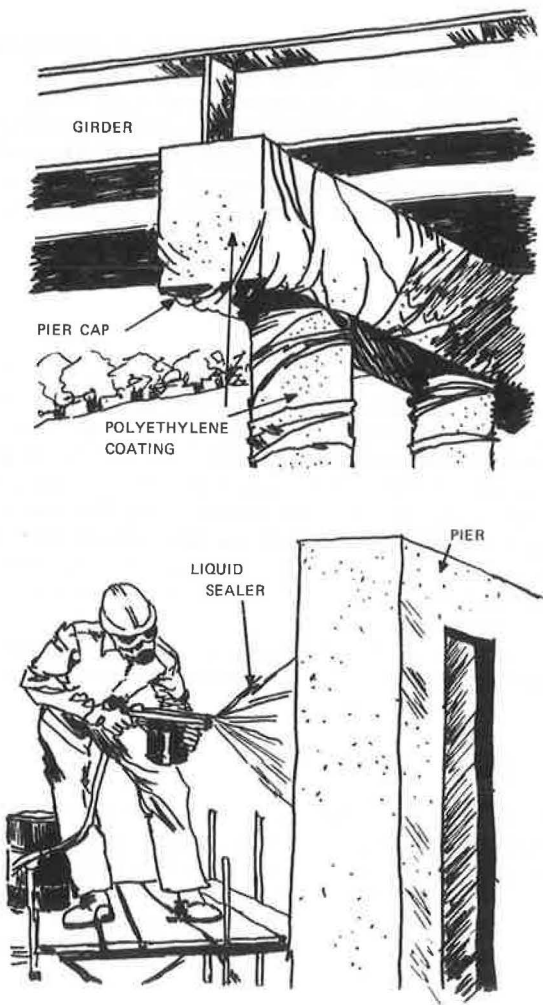Figure 1. Composition of broad red and gray stains.

Figure 2. Temporary stain protection.

a combination of sodium citrate and sodium hydrosulfite for removing iron stains. This method, however, is expensive and time consuming.

Red and gray stains, which make up more than 75 percent of the stains on most bridges, were relatively easy to remove. An estimated 95 percent of these stains were removed from the Seventh Street overpass of I-40 in North Little Rock, Arkansas, by washing with a brush, cleaning agent, and rinse water. Use of a dry brush alone removed 60 percent of the stain. Application of Removox, a mixture of hydrochloric acid, gluconic acid, 9-10 molar ethylene oxide nonionic, 12-15 molar ethylene oxide nonionic, and an inhibitor, also removed 90 to 95 percent of the stain with or without brushing. This cleaning agent, because of the acid it contains, also removes some of the concrete matrix.

Prevention of Stains

Prevention of stains, other than graffiti, is accomplished by keeping water off the concrete. The most effective method is to use continuous-span bridges or to place the expansion joint away from the bridge piers. Elimination of expansion joints over bridge piers, however, is not always economical.

A 1973 Georgia Department of Transportation study (3) of bridge expansion joints concludes that joints can be sealed by sealing the vertical curb face at construction joints. Specifying use of sliding plate joints, preformed seals (with high solids adhesive), and armored joints could be discontinued.

Coatings and sealers are effective in preventing stains over short periods of time (Figure 2) (4). Polyethylene and vinyl can effectively prevent stains during the construction period before the bridge deck is poured. With time, however, coatings and sealers break down and expose the concrete to stains.

A sloping abutment with drain (Figure 3) is effective for eliminating stains from bridge ends (4). Drip pans, also shown in Figure 3, are only moderately successful because the wind that accompanies storms will blow water on the bridge piers.

Expansion joints between sections of bridges can effectively be sealed in 1 of 3 ways (Figure 4). Where expansions are large, as in finger joints, the neoprene or conveyor-belt trough is effective. Veral Pinkerton of the Arkansas Highway Department has stated that care must be taken to ensure that the belt trough has sufficient room to flex so that it will not become clogged. Intermediate movements can be absorbed with angle troughs, and small expansions can be absorbed with compressible, preformed joint sealers. Compressible joint sealers must be installed with care or leaks will develop.

CONCLUSIONS

Stains on bridges in Arkansas were not damaging to the structures.

Natural stain, that is, all stains except graffiti, were the result of weathering and and surface runoff.

Natural stains, other than rust stains, can be removed effectively by sandblasting; washing with soap, water and a brush; or applying certain acids and rinsing. These stains will recur, however, unless their source is found and corrected.

Bridge pier stains can be reduced greatly by preventing rainfall runoff from reaching the concrete below the bridge deck.

ACKNOWLEDGMENT

Figure 3. Abutment protection and drip pan.

GIRDER

DRIP PAN

END DAM

GIRDER

DRY WELL

SEAT

DRAIN INSIDE PIER

SLOPING ABUTMENT

Figure 4. Expansion joint protection.

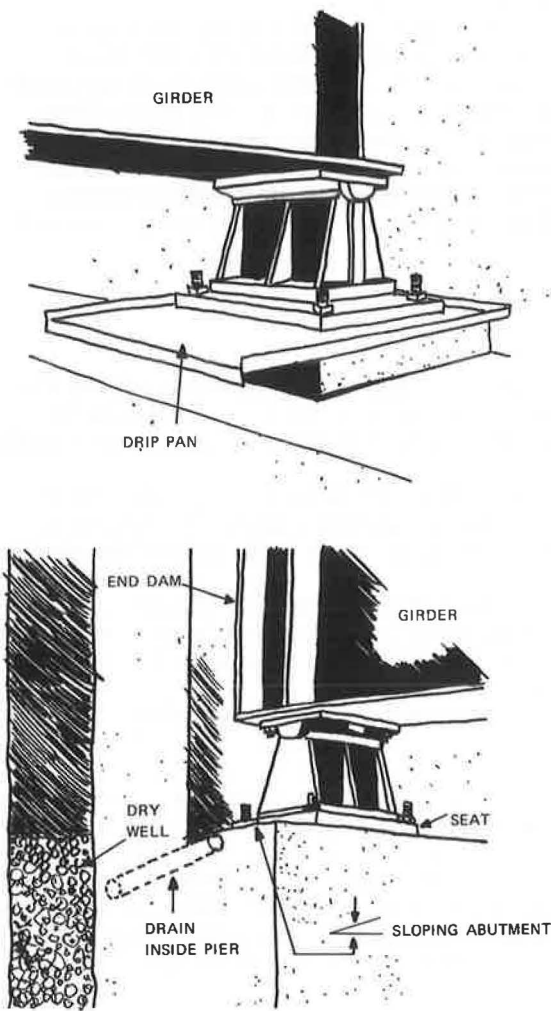TOOTH PLATE   TROUGH   SPLASH PLATE   TOOTH PLATE

GIRDER   GIRDER

PIER

COMPRESSIBLE SEALER
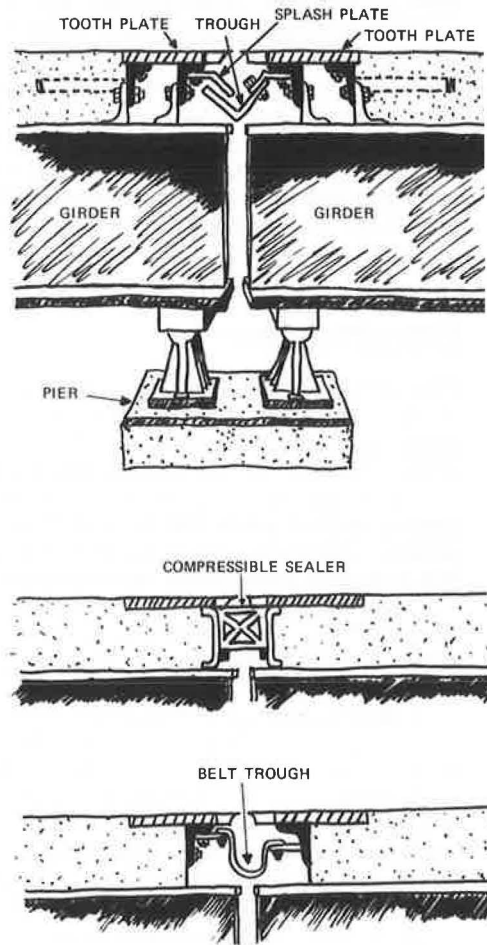
BELT TROUGH

REFERENCES

1. S. I. Thornton and C. Springer.   Causes of Bridge Pier Staining.   Arkansas Highway Department, Highway Research Project 33, Final Rept., Feb. 1974.
2. C. R. Derrington, R. L. Stowe, and W. G. Miller.   Investigation of Methods for Removing Stains From Mortar and Concrete.   U.S. Army Engineer Waterways Experiment Station, Vicksburg, Mississippi, Miscellaneous Paper C-68-8, Oct. 1968.
3. J. B. Thornton.   Evaluation of Existing Bridge Expansion Joints.   Office of Materials and Test, Georgia Department of Transportation, Research Project 7112, Final Rept., Oct. 1973.
4. Mayari R.   Booklet 2858, Public Affairs Department, Bethlehem Steel Corp.

SPONSORSHIP OF THIS RECORD

GROUP 2—DESIGN AND CONSTRUCTION OF TRANSPORTATION FACILITIES
W. B. Drake, Kentucky Department of Transportation, chairman

STRUCTURES SECTION
Arthur L. Elliott, California Department of Transportation, chairman

Committee on General Structures
W. J. Wilkes, Federal Highway Administration, chairman
Frank D. Sears, Federal Highway Administration, secretary
William L. Armstrong, N. H. Bettigole, Martin P. Burke, Jr., Daniel E. Czernik,
Arthur L. Elliott, Donald C. Frederickson, George G. Goble, William A. Kline, Heinz
P. Koretzky, Robert M. Olson, Adrian Pauw, Wendell M. Smith

Committee on Steel Bridges
Gerard F. Fox, Howard, Needles, Tammen and Bergendoff, chairman
John W. Fisher, Lehigh University, secretary
Russell L. Chapman, Jr., Arthur L. Elliott, Richard S. Fountain, T. V. Galambos,
C. H. Gronquist, Wayne Henneberger, Theodore R. Higgins, William A. Kline, W. H.
Munse, Frank D. Sears, A. A. Toprac, I. M. Viest, Charles H. Wilson

Committee on Concrete Bridges
Cornie L. Hulsbos, University of New Mexico, chairman
T. Alberdi, Jr., Hotten A. Elleby, John M. Hanson, Norris L. Hickerson, David S.
Huval, Francis J. Jacques, Walter J. Jestings, George F. Leyh, Charles C. Mitchell,
Joseph H. Moore, Robert A. Norton, Emile G. Paulet, Dominick L. Somma, David A.
Van Horn, Earle E. Wilkinson

GROUP 3—OPERATION AND MAINTENANCE OF TRANSPORTATION FACILITIES
Lloyd G. Byrd, Byrd, Tallamy, MacDonald, and Lewis, chairman

Committee on Structures Maintenance
Abel R. Sirois, Maine Department of Transportation, chairman
Harvey H. Shafer, Dow Center Laboratory 9, secretary
Roland H. Berger, Myron G. Brown, William M. Cheatham, Robert C. Donnaruma,
Karl H. Frank, D. R. Higgins, Leonard L. Ingram, Gayle E. Lane, Robert A. Martin,
Stephen E. Roberts, Vernon W. Smith, Jr., John C. Volk, Jr., Alden L. West, Robert
L. Whissen

Lawrence F. Spaine and Adrian Clary, Transportation Research Board staff

Sponsorship is indicated by a footnote on the first page of each report. The organizational units and the chairmen and members are as of December 31, 1974.